THE SECOND HARMONIC GENERATION IN REFLECTION MODE - AN ANALYTICAL, NUMERICAL AND EXPERIMENTAL STUDY

A Thesis
Presented to
The Academic Faculty

by

Anne Romer

In Partial Fulfillment
of the Requirements for the Degree
Master of Science in Engineering Science and Mechanics in the
School of Civil and Environmental Engineering

Georgia Institute of Technology
December 2014

THE SECOND HARMONIC GENERATION IN REFLECTION MODE - AN ANALYTICAL, NUMERICAL AND EXPERIMENTAL STUDY

Approved by:

Professor Laurence J. Jacobs, Advisor
School of Civil and Environmental Engineering
Georgia Institute of Technology

Dr. Jin-Yeon Kim
School of Civil and Environmental Engineering
Georgia Institute of Technology

Dr. Jianmin Qu
Department of Civil and Environmental Engineering
Northwestern University

Date Approved: 22. August 2014

ACKNOWLEDGEMENTS

First, I would like to thank my advisor Professor Laurence J. Jacobs for supporting me throughout my graduate studies, for the help regarding all kind of problems and for giving me the opportunity to take part in the Quantitative Nondestructive Evaluation conference in Boise. Furthermore I want to thank Dr. Jin-Yeon Kim for helpful inputs throughout my thesis and for useful discussions and ideas. Thanks goes to Dr. Jianmin Qu from Northwestern University for serving as a committee member and reviewing this thesis. I also want to thank Prof. Lothar Gaul, Christian Ehrlich and all the persons who make that ISAP exchange program possible.

Besides I want to thank all the labmates for the nice and helpful atmosphere and also my predecessors for their answers and their help. Special thanks goes to Daniel Marino and Florian Morlock for sharing joy and sorrow during this year in the United States.

Furthermore I am grateful for being financially supported by the Deutscher Akademischer Austauschdienst (DAAD) and the Studienstiftung des deutschen Volkes.

Moreover I want to thank my family who exceptionally supported me in the last years.

TABLE OF CONTENTS

ACKNOWLEDGEMENTS . . . . . **iii**

LIST OF TABLES . . . . . **vi**

LIST OF FIGURES . . . . . **vii**

LIST OF SYMBOLS OR ABBREVIATIONS . . . . . **xii**

SUMMARY . . . . . **xiii**

I INTRODUCTION **1**

1.1 Motivation 1

1.2 Objective 4

1.3 Outline 4

II FUNDAMENTALS OF WAVE PROPAGATION IN SOLIDS **5**

2.1 Linear Wave Propagation 5

2.1.1 Linear equations of motion 5

2.1.2 P-wave and S-wave 7

2.1.3 Refraction, Reflection and Transmission 8

2.2 Nonlinear Wave Propagation 10

2.2.1 Nonlinear Wave Equation 10

2.2.2 Perturbation Method 12

2.2.3 Bulk interaction of elastic waves 13

2.2.4 Solution of the Equation of Motion 15

2.2.5 Boundary Conditions 17

III SECOND HARMONIC GENERATION AT A FREE BOUNDARY . **18**

3.1 Primary wave field 18

3.2 Secondary wave field 20

3.2.1 Transmitted P-wave 20

3.2.2 Transmitted S-wave 23

3.3 Model analysis for different parameters 23

IV SIMULATIONS - FINITE ELEMENT MODEL 30
4.1 Modeling 30
4.1.1 Geometry 30
4.1.2 Material 31
4.1.3 Physics and boundary conditions 33
4.1.4 Mesh size, time steps and solver 34
4.2 Simulation 35
4.2.1 Computation 35
4.2.2 Signal Processing 35
4.3 First results and necessary improvements 37
4.3.1 Results of the standard model 37
4.3.2 Avoidance of surface waves 40
4.3.3 Avoidance of interaction with diffracted P-wave at position 4 . . . 43
4.4 Confirmation of the finite element model 45
V RESULTS OF THE SIMULATIONS 46
5.1 FEM results for suggested measurement model 46
5.2 Robustness regarding Hann window variations 47
5.3 Robustness regarding receiver position variations 50
5.4 Recommendation for experimental setup 51
5.4.1 Receiver position 51
5.4.2 Incident angle 53
VI EXPERIMENTS 56
6.1 Experimental Setup 56
6.1.1 Specimens 59
6.2 Experimental Results 59
6.2.1 Absolute nonlinearity value 65
VII CONCLUSION AND FUTURE WORK 67
7.1 Conclusion 67
7.2 Outlook 68
REFERENCES 69

LIST OF TABLES

3.1 Material properties of Acrylic Plastic 19

3.2 Material properties of Aluminum 20

3.3 Summary of the secondary wave field considering only the transmitted P-wave 22

3.4 Summary of the secondary wave field considering only the transmitted S-wave 23

6.1 Possible measurement setup values 61

6.2 Relative nonlinearity parameter obtained by using the reflection at a stress-free boundary 63

6.3 Resulting nonlinearity ratio in comparison with literature values 64

LIST OF FIGURES

1.1 Reactor pressure vessel [10] as an example for an in-service NDE application 3

1.2 Possible experimental setup using reflection at a stress-free boundary at a) normal incidence and b) oblique angle 3

2.1 Reflection and transmission of a P- and S-wave at a solid-solid interface . . 9

2.2 Solution procedure for solving the nonlinear equations of motion 14

2.3 Coordinate system of the infinite half-space 16

3.1 Investigated setup with reflection of an initial P- and S-wave at a stress-free boundary 19

3.2 Normalized amplitude of transmitted and reflected waves 21

3.3 Amplitudes of the reflected primary waves 21

3.4 Superposition of the secondary wave field of the transmitted P- and S-wave for different angles 25

3.5 Comparison of the secondary wave field of the transmitted P- and S-wave for $\Theta_P = 20°$ and $\Theta_P = 70°$ 26

3.6 Generated second harmonic wave field plotted over different values of TOECs, thickness and generated incident amplitude for different angles 27

3.7 Generated second harmonic wave field plotted over arriving fundamental waves for increased TOECs 28

3.8 Generated second harmonic wave field over different angles 29

4.1 FE simulation model with material, physics and boundary conditions 31

4.2 Normalized prescribed displacement 33

4.3 Amplitude of prescribed displacement of the transducer plotted over the boundary section 34

4.4 Signal processing of the simulation results 36

4.5 X- and y-component of the displacement field in the time domain at position 4, position 5, position 1 and position 2 38

4.6 X- and y-component of the displacement field in the frequency domain at position 4, position 5, position 1 and position 2 plotted over all relevant frequencies in A and zoomed in for the second harmonic amplitude in B . . 39

4.7 Y-component of the displacement field of the stress-free surface boundary at two different times revealing two surface waves 40

4.8 Y-component of displacement field of the specimen showing a Rayleigh surface wave originating at time $t = 1.5e - 5$ s 41

4.9 Y-component of displacement field of the specimen showing a Rayleigh surface wave propagating at time $t = 2.5e-5$ s 42

4.10 Y-component of displacement field of the specimen at time $t = 1.5e-5$ s with a long wedge preventing the Rayleigh wave from originating 42

4.11 Displacement field at position 4 in the time domain and in the frequency domain for a) setup with short wedge, where a Rayleigh surface wave is generated and b) setup with long wedge 43

4.12 Illustration of L_{min} in order to avoid interaction with diffracted waves . . . 44

4.13 Maximum cycles n_{max} for a given thickness L 45

4.14 Displacement field at position 4 in the time domain for a) n=15 and b) n=12 cycles of generated sinus oscillations 45

5.1 Second harmonic amplitude plotted over the generated incident amplitude . 48

5.2 Arriving second harmonic amplitude divided by the arriving fundamental amplitude plotted over the incident amplitude 48

5.3 Linear fit of second harmonic amplitude plotted over squared fundamental amplitude 49

5.4 Comparison of linear fit of A_2/A_1^2 in y-direction at position 4 and position 5 49

5.5 Second harmonic amplitude plotted over the generated incident amplitude with varying Hann window regarding only y-components 50

5.6 Linear fit of second harmonic amplitude plotted over squared fundamental amplitude with varying Hann window regarding only y-components 51

5.7 Second harmonic amplitude plotted over the generated incident amplitude with shifted receiver regarding only y-components 52

5.8 Linear fit of second harmonic amplitude plotted over squared fundamental amplitude with shifted receiver regarding only y-components 52

5.9 Second harmonic amplitude and fundamental amplitude plotted over increasing angles of the P-wave 54

5.10 A_2/A_1^2 plotted over increasing propagation distance 55

6.1 Experimental approach 57

6.2 Experimental setup 58

6.3 Signal processing of the experimental data 58

6.4 Measured time domain signal at position 5 60

6.5 Measured time domain signal at position 4 60

6.6 Linear fit of measured amplitudes A_2 to A_1^2 in order to determine the slope 62

6.7 Comparison of the robustness of the relative β^{rel} values at position 5 and position 4 for Al 2024 62

6.8 Comparison of the relative nonlinearity parameter of Al 2024 and Al 7075 obtained by using the reflection at a stress-free boundary 63

6.9 β^{rel} value measured using different incident angles plotted over propagation distance 64

LIST OF SYMBOLS OR ABBREVIATIONS

Symbol	Description
$\alpha^{surf}, \gamma^{surf}$	surface parameters
β^{bulk}	bulk parameter
δ_{ij}	Kronecker delta
ϵ_{ij}	linear strain tensor
Θ_i	incident angle of generated incident wave
Θ_P	angle corresponding to a P-wave in the specimen
Θ_S	angle corresponding to a S-wave in the specimen
Θ_{cr}	critical angle
λ	Lamé's first parameter
μ	Lamé's second parameter
ν	Poisson's ratio
ρ	mass density
σ_{ij}	linear stress tensor
Φ, Ψ	angles for second harmonic waves generated by cross-interaction
ϕ, ψ	scalar and vectorial potentials
ω	angular frequency
A	wave amplitude
A_1, A_2	fundamental and second harmonic wave amplitude
A_i	wave amplitude of the generated incident P-wave
$A_{Pt}, A_{St}, A_{Pr}, A_{Sr}$	wave amplitude of the transmitted P- or S-wave, wave amplitude of the reflected P- or S-wave
B_1, B_2, C_1, C_2, C_3	constants used in solution process
$\mathcal{A}, \mathcal{B}, \mathcal{C}$	third order elastic constants according to Landau
c_0	wave velocity (either c_P or c_S)

Symbol	Description
c_P, c_S	longitudinal, shear wave velocity
$\mathbf{d}$	unit vector in direction of displacement
$\mathbf{E}$	Lagrangian strain tensor
E	Young's modulus
f	frequency
f_i	body force
i	imaginary unit
$\mathbf{k}$	wave vector
$\mathbf{k_P}, \mathbf{k_S}$	longitudinal, shear wave vector
k	wave number
k_P, k_S	longitudinal, shear wave number
L	thickness of specimen
n	number of generated cycles of sinus oscillation
n_i	outward normal unit vector on surface
$\mathbf{P}$	first Piola-Kirchhoff stress tensor
$\mathbf{P}^L, \mathbf{P}^{NL}$	Linear, nonlinear part of $\mathbf{P}$
$\mathbf{p}$	unit vector of propagation direction
S	surface of closed region
t_i	surface traction
t	time
$\mathbf{u}$	displacement field
$\mathbf{u}^{(1)}, \mathbf{u}^{(2)}$	primary, secondary wave field
V	volume of closed region
$\mathbf{x}$	position vector
$x_1, x_2, x_3 = x, y, z$	Cartesian coordinates in the reference configuration

Abbreviation	Denotation
BVP	boundary value problem
DFT	discrete Fourier transform
DPP	domain point probe
FEM	finite element method
FE	finite element
NDE	nondestructive evaluation
P-wave	pressure wave
PACE	partnership for an advanced computing environment
S-wave	shear wave
TOEC	third order elastic constant

SUMMARY

Implementation of the ultrasonic second harmonic generation has typically been restricted to simple setups such as through-transmission or Rayleigh surface waves. Recent research has evaluated the second harmonic generation in P- and SV- waves reflected from a stress-free surface to enable the single-sided interrogation of a specimen. This research considers the second harmonic generation in an aluminum specimen, which is analytically evaluated using an approach based on the perturbation method. Here, the model is chosen to mimic an experimental setup where a longitudinal wave is generated at an oblique angle and the reflected wave is detected using a set of wedge transducers. Due to mode conversion at the interface of the wedge and the specimen, it is necessary to evaluate longitudinal and shear waves, determining all second harmonic waves generated in the bulk and at the stress-free boundary. The theoretically developed model is then implemented in a commercial finite element code, COMSOL, using increasing fundamental wave amplitudes for different values of third order elastic constants. The results of this computational model verify the analytical approach and the proposed measurement setup, taking into account assumptions and approximations of the solution procedure. Furthermore, the computational model is used to draw important conclusions relevant to the experimental setup, including the need to avoid evolving surface waves and interactions with diffracted waves. These numerical results are used to develop a recommendation for the measurement position and incident angle. Finally, the nonlinearity of two different aluminum specimens is measured with the suggested measurement setup and the results confirm the feasibility of the single-sided determination of the acoustic nonlinearity using reflected bulk waves.

CHAPTER I

INTRODUCTION

This chapter introduces the fundamentals and the applications of nonlinear ultrasonics in nondestructive evaluation (NDE), and the research objective of this work is prescribed. An overview of existing literature is given and related results are discussed. Finally, this chapter is completed by an outline of the entire thesis.

1.1 Motivation

In the last decades, ultrasonic technology has proven to be a useful field NDE technique to assess the state of materials. Determining the damage state of critical components can reduce maintenance costs and secure a higher level of safety. However, conventional linear ultrasonic technology is only capable of detecting macroscopic cracks or determining stiffness parameters, but can not provide quantitative information about material state such as residual stress or strength parameters, as well as before the formation of macrocracks. Therefore, it is desirable to develop methodologies capable of assessing the state of a material throughout its entire life cycle. In recent years nonlinear ultrasonics has shown great potential to monitor the fatigue life and the accumulation of damage in the material rather than waiting for macroscopic cracks to form. This is possible because the nonlinear ultrasound is sensitive to microstructural changes associated with dislocations. Several researchers have linked these changes to mechanical, thermal, and radiation damage [8, 18, 22, 26].

Nonlinear ultrasonic techniques often measure the higher harmonics due to the nonlinear material properties to draw conclusions about the state of a component. For weakly nonlinear materials such as metals, generally only the second harmonic waves will be large enough to provide repeatable results.

Existing measurement setups for the second harmonic generation usually determine the material nonlinearity using bulk waves in the through transmission mode [22, 26], Rayleigh waves [18, 30] or Lamb waves [6, 28]. However, there are some drawbacks in each of these

measurement approaches. Through transmission measurements using bulk waves requires access to both sides, which is often not possible with in-service components. Rayleigh waves only interrogate the surface of a component to the depth of one wavelength, which is usually less than a few millimeters. Finally, Lamb waves are limited in their applications since very few modes fulfill the requirements for cumulative propagation [28]. Furthermore, Rayleigh as well as Lamb waves need a minimum propagation distance, and most importantly the resulting measured material nonlinearity is an average over the propagation distance, and can not be localized.

A measurement setup using bulk wave reflection at a stress-free boundary can potentially provide information about the local state throughout the thickness of an in-service component such as a reactor pressure vessel illustrated in Figure 1.1. This can be a great advantage for monitoring in-service components throughout their lifetime for higher safety. A mathematical solution for the second harmonic generation from a reflected wave was studied in [5, 34, 35] amongst others, where Bender et al. [5] and Zhou et al. [35] focused on the stress-free boundary.

Best et al. [7] provide simulations and experimental data that show the potential of nonlinear measurements with reflection at a stress-free boundary to be an alternative to the usual through-transmission setup. They use the pure normal incidence as illustrated in Figure 1.2 a) where the wave propagates perpendicular to the stress-free surface. Neglecting attenuation and diffraction, the second harmonic wave generated during forward propagation will theoretically decrease to zero upon reflection from a stress-free surface due to the 180° phase shift of the primary wave at the stress-free boundary [5, 7, 31, 32]. Therefore, only a small amplitude of the second harmonic wave compared to the amplitude of the first harmonic wave can be measured with normal incidence. Best et al. [7] increase the second harmonic amplitude by beam forming and frequency optimization. However, an incident angle that is not normal to the stress-free surface leads to a higher second harmonic amplitude. Therefore, a measurement setup with reflection at a stress-free boundary at an oblique angle, as illustrated in Figure 1.2, is investigated in this thesis.

Figure 1.1: Reactor pressure vessel [10] as an example for an in-service NDE application

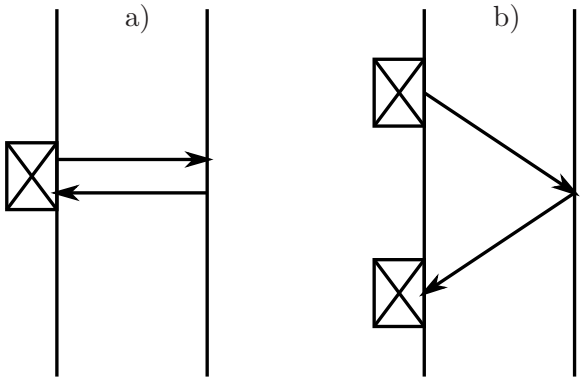

Figure 1.2: Possible experimental setup using reflection at a stress-free boundary at a) normal incidence and b) oblique angle

1.2 Objective

The objective of this research is to formulate, evaluate and experimentally test potential experimental setups that use second harmonic generation in the reflection mode. The first step is to understand, model and simulate how second harmonic waves are generated in the reflection mode. This step utilizes existing mathematical solutions to develop an analytical model of the second harmonic generation at a stress-free surface. Then a numerical model is developed to validate the analytical results. These results are used to formulate potential measurement setups, where each case can be numerically and experimentally evaluated. Finally the proposed experimental configurations are used to experimentally measure the material nonlinearity of a specimen using the reflection from a stress-free boundary.

1.3 Outline

The structure of the thesis is as follows: An introduction into the fundamentals of wave propagation, that are relevant to this research, will be given in Chapter 2. In Chapter 3, these concepts will be used to formulate a possible measurement setup and analyze the generation of the second harmonic waves analytically. On the basis of the evaluated measurement setup a numerical model is developed in Chapter 4 and important criteria for an experimental setup are drawn. In Chapter 5 the numerical and the analytical results are compared and the possible measurement setup is evaluated. Hereupon, an experimental procedure is presented and the feasibility of the suggested measurement setup is validated experimentally in Chapter 6. Finally a conclusion and an outlook for future works are given in Chapter 7.

CHAPTER II

FUNDAMENTALS OF WAVE PROPAGATION IN SOLIDS

In this chapter the fundamentals of linear wave propagation in solids are presented. It starts with the basics of linear wave propagation including the linear equations of motion with the final focus on the refraction and reflection of linear waves. This is followed by the introduction of the nonlinear wave propagation theory. The nonlinear wave equation is then solved at the presence of a stress-free boundary. The mathematical background that is provided in the following chapter can be found in various books and other publications [1, 4, 17, 23, 27].

2.1 Linear Wave Propagation

In the following linear constitutive and geometric relations are applied to derive the linear elastic equation of motion. As result of the equation of motion the P- and S-waves are discussed as well as transmission and reflection of P- and S-waves.

2.1.1 Linear equations of motion

In order to derive the equations of motion for an elastic solid, we start with the balance of linear momentum, which states that the time rate of change of the total momentum of a free body equals the vector sum of all external forces.

$$\int_V \rho \ddot{u}_i dV = \int_S t_i dS + \int_V f_i dV \tag{1}$$

Here S is the surface area, V is the volume, u_i is the displacement, t_i is the traction and f_i represents the body force. The traction t_i can be expressed by Cauchy's formula

$$t_i = \sigma_{ij} n_j \tag{2}$$

where σ_{ij} is the Cauchy-Stress-Tensor and n_j represents the outward normal unit vector. One can now plug Cauchy's formula into Equation (1) and transform the surface integral to

a volume integral by using the divergence theorem. Rearranging terms to one side finally yields to

$$\int_V (\partial_j \sigma_{ij} - \rho \ddot{u}_i + \rho f_i) dV = 0 \tag{3}$$

Since this equation is valid for arbitrary V, one can conclude

$$\partial_j \sigma_{ij} + \rho f_i = \rho \ddot{u}_i \tag{4}$$

which is known as Cauchy's equations of motion. Applying the principle of angular momentum, Cauchy's stress tensor σ_{ij} turns out to be symmetric.

For homogeneous, isotropic and linear elastic medium the relationship between stress σ and strain ϵ is given by

$$\sigma_{ij} = \lambda \epsilon_{kk} \delta_{ij} + 2\mu \epsilon_{ij} \tag{5}$$

with the two second-order elastic constants λ and μ, also known as Lamé constants. The strain tensor ϵ_{ij} can be expressed in terms of the displacement u_i

$$\epsilon_{ij} = \frac{1}{2}(\partial_j u_i + \partial_i u_j) \tag{6}$$

which leads to the expression of Cauchy's stress tensor

$$\sigma_{ij} = \lambda u_{kk} \delta_{ij} + \mu(\partial_j u_i + \partial_i u_j) \tag{7}$$

Substituting Cauchy's stress tensor in Equation 5, we obtain

$$(\lambda + \mu)\partial_j \partial_i u_j + \mu \partial_j \partial_j u_i = \rho \ddot{u}_i \tag{8}$$

or in vector representation

$$(\lambda + \mu)\nabla \nabla \mathbf{u} + \mu \nabla^2 \mathbf{u} = \rho \ddot{\mathbf{u}} \tag{9}$$

Note that body forces are neglected. Applying the Helmholtz decomposition the vector field $\mathbf{u}$ can be decomposed into

$$\mathbf{u} = \nabla \phi + \nabla \times \psi \;\text{ with }\; \nabla \cdot \psi = 0 \tag{10}$$

by using a scalar potential ϕ and a vector potential ψ. For this decomposition to be valid, the zero-divergence condition for the vector potential is necessary in order to decompose

the components of **u** uniquely. When we substitute Equation (10) in Equation (9) we get two uncoupled wave equations in terms of the scalar potential ϕ and the vector potential ψ.

$$\nabla^2\phi - \frac{1}{c_p^2}\ddot{\phi} = 0 \text{ and } \nabla^2\psi - \frac{1}{c_s^2}\ddot{\psi} = 0 \tag{11}$$

Here $c_p = \sqrt{(\lambda + 2\mu)/\rho}$ and $c_s = \sqrt{\mu/\rho}$ holds.

2.1.2 P-wave and S-wave

In this section the phenomena resulting of the derived wave equation are presented. Here the P-wave and S-wave, also called the bulk waves, are covered as they are later analyzed at the stress-free boundary. Note that in this section only plane waves are considered, where the wavefronts with uniform displacements occur on parallel planes standing vertically on the direction of propagation.

We regard two cases: the curl free displacement field where $\phi = 0$ and the divergence free displacement field where $\psi = 0$. The case of $\phi = 0$ results in the wave traveling with the speed c_p^2 that is called dilatational, irrotational, primary, longitudinal, pressure or P-wave. In the divergence free displacement field we obtain a wave that travels with speed c_s^2 and is called transversal, rotational, distortional, secondary, shear or S-wave.

The general three dimensional plane wave solution is given by

$$\mathbf{u} = A\mathbf{d}f(\mathbf{p}\cdot\mathbf{x} - ct) \tag{12}$$

with the amplitude A, the unit vector in the direction of displacement **d**, the unit vector in the direction of propagation **p**, the wave speed c, time t and the position x. By substituting Equation (12) into Equation (9) we obtain

$$(\mu - \rho c^2)\mathbf{d} + (\lambda + \mu)(\mathbf{p}\cdot\mathbf{d})\mathbf{p} = 0 \tag{13}$$

Since **p** and **d** are two different unit vectors, we can conclude that there are two possible solutions $\mathbf{d} = \pm\mathbf{p}$ or $\mathbf{p}\cdot\mathbf{d} = 0$. In the first case $\mathbf{d} = \pm\mathbf{p}$ leads to $\mathbf{p}\cdot\mathbf{d} = \pm 1$. This results in $c = c_p$, the wave speed of the P-wave. Since **p** and **d** are linearly dependent, the propagation direction of a P-wave is also the direction of its displacement. This explains why the P-wave is also called longitudinal wave.

In the second case $\mathbf{p}\cdot\mathbf{d} = 0$ shows that the direction of wave propagation is perpendicular to the direction of the displacement amplitude. Evaluating Equation (13) in this case results in $c = c_s$, the wave speed of the S-wave. The perpendicular polarization of the displacement explains why the S-wave is also called the transversal wave. Note that in a two-dimensional plane of propagation the S-wave is sub-divided into two types, the vertically polarized S-wave or SV-wave with in-plane displacement and the horizontally polarized S-wave or SH-wave with out-of-plane displacement. Since in this thesis the model is only two dimensional, only the SV-wave is considered. Thus, the term S-wave denotes SV-wave in general.

In the following chapters the representation of a plane harmonic displacement wave is chosen to be

$$\mathbf{u} = A\mathbf{d}\cos(\omega t - \mathbf{k}\cdot\mathbf{x}) \tag{14}$$

where $\mathbf{k}$ is the wave vector pointing in the direction of propagation, $k = \|\mathbf{k}\|$ is defined as the wave number and $\omega = ck$ is the constant angular frequency. It can be seen that this representation fulfills the definition of plane waves of Equation (12).

Another notation used is

$$\mathbf{u} = A\mathbf{d}e^{j(\omega t - \mathbf{k}\cdot\mathbf{x})} \tag{15}$$

where only the real part of the term represents the physical wave such that it correlates with Equation (14). Using this representation one has to keep in mind that taking the real part is a linear operator. Therefore, taking the real part has to be applied to the primary waves as stated in [4].

2.1.3 Refraction, Reflection and Transmission

In order to later evaluate the second harmonic generation in the presence of the stress-free boundary, the phenomena of refraction, reflection and transmission of the primary wave at an oblique angle must be considered. In this thesis the solution to the most general case is presented. This solution can then be simplified to arbitrary interfaces. For the derivation of the following solution or for further reading the reader is referred to [2] or [17].

This most general case is represented by a solid-solid interface for an arbitrary incident wave, as illustrated in Figure 2.1.

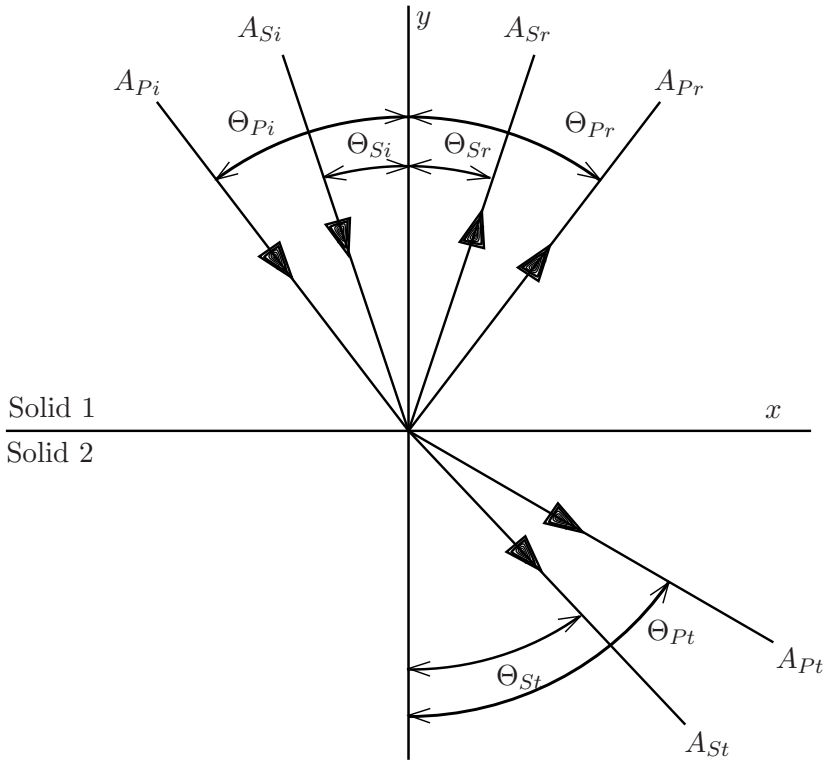

Figure 2.1: Reflection and transmission of a P- and S-wave at a solid-solid interface

From Snell's law, we know

$$\frac{\sin(\Theta_{Pi})}{c_{P1}} = \frac{\sin(\Theta_{Si})}{c_{S1}} = \frac{\sin(\Theta_{Pr})}{c_{P1}} = \frac{\sin(\Theta_{Pt})}{c_{P2}} = \frac{\sin(\Theta_{Sr})}{c_{S1}} = \frac{\sin(\Theta_{St})}{c_{S2}} \tag{16}$$

where second index of the wave velocities represent solid 1 or solid 2 respectively. Evaluating the boundary conditions, which state that normal and transverse velocity as well as the stress components are continuous at the interface, one obtains following formula for the

reflected and transmitted amplitudes in case of an incident P or S-wave

$$\begin{pmatrix} -\cos\theta_{Pr} & -\cos\theta_{Pt} & -\sin\theta_{Sr} & \sin\theta_{St} \\ -\sin\theta_{Pr} & \sin\theta_{Pt} & \cos\theta_{Sr} & \cos\theta_{St} \\ -Z_{P1}\cos 2\theta_{Sr} & -Z_{d2}\cos 2\theta_{Sr} & -Z_{s1}\sin 2\theta_{Sr} & -Z_{S2}\sin 2\theta_{St} \\ -Z_{P1}\frac{c_{S1}}{c_{P1}}\sin 2\theta_{Pr} & -Z_{S2}\frac{c_{S2}}{c_{P2}}\sin 2\theta_{Pt} & Z_{S1}\cos 2\theta_{Sr} & -Z_{S2}\cos 2\theta_{St} \end{pmatrix} \begin{pmatrix} A_{Pr} \\ A_{Pt} \\ A_{Sr} \\ A_{St} \end{pmatrix} = \begin{pmatrix} -\cos\theta_{Pi}A_{Pi} \\ \sin\theta_{Pi}A_{Pi} \\ Z_{P1}\cos 2\theta_{Pi}A_{Pi} \\ -Z_{S1}\frac{c_{S1}}{c_{P1}}\sin 2\theta_{Pi}A_{Pi} \end{pmatrix} \quad \text{or} \quad = \begin{pmatrix} \sin\theta_{Si}A_{Si} \\ \cos\theta_{Si}A_{Si} \\ -Z_{S1}\sin 2\theta_{Si}A_{Si} \\ -Z_{S1}\cos 2\theta_{Si}A_{Si} \end{pmatrix} \tag{17}$$

Note that this solution can easily be simplified to obtain the reflection of an incident P- or S-wave at a stress-free boundary.

2.2 Nonlinear Wave Propagation

In the linear problem quadratic and higher order terms are neglected. But especially the generation of higher harmonic waves due to material nonlinearities are useful for nondestructive evaluation of materials. Nonlinear techniques have the potential to monitor the gradual accumulation of damage in a material before the initiation of a crack. Therefore, important nonlinear concepts are discussed in this chapter starting with the nonlinear wave equation based on finite deformation. This concepts is used to evaluate the interaction of elastic waves. Finally the boundary conditions are introduced.

2.2.1 Nonlinear Wave Equation

In case of finite deformation the Piola-Kirchhoff stress tensor P_{ij} is applied to express the stresses relative to the reference configuration. The nonlinear equations of motion can then be expressed by using this stress tensor in Cauchy's first law of motion of Equation (4) with body forces neglected:

$$\rho\ddot{u}_i = \partial_j P_{ji} \tag{18}$$

The Piola-Kirchhoff stress tensor P_{ij} is given by

$$\begin{aligned} P_{ij} &= \lambda \partial_k u_k \delta_{ij} + \mu(\partial_j u_i + \partial_i u_j) \\ &+ (\frac{1}{2}\lambda \partial_l u_k \partial_l u_k + \mathcal{C}\partial_k u_k \partial_l u_l)\delta_{ij} + \mathcal{B}\partial_k u_k \partial_j u_i + \frac{1}{4}\mathcal{A}\partial_k u_i \partial_j u_k \\ &+ \frac{1}{2}\mathcal{B}(\partial_l u_k \partial_l u_k + \partial_l u_k \partial_k u_l)\delta_{ij} + (\lambda + \mathcal{B})\partial_k u_k \partial_i u_j \\ &+ (\mu + \frac{1}{4}\mathcal{A})(\partial_k u_j \partial_k u_i + \partial_j u_k \partial_i u_k + \partial_k u_j \partial_i u_i) \end{aligned} \tag{19}$$

in terms of the displacement u_i and the third order elastic constants (TOECs) $\mathcal{A}$, $\mathcal{B}$ and $\mathcal{C}$ introduced by Landau and Lifshitz [23]. Note that there are different ways to express these TOECs. The use and conversion of the TOECs are presented and explained in [9], [11] and [15] amongst others. The derivation to obtain the stated formula can be found in [23]. Note that this expression of P_{ij} can be decomposed into a linear part that equals the expression for the Cauchy stress tensor (7) and a nonlinear part of second order in u_i:

$$P_{ij} = P_{ij}^L + P_{ij}^{NL} \tag{20}$$

with

$$P_{ij}^L = \lambda \partial_k u_k \delta_{ij} + \mu(\partial_j u_i + \partial_i u_j) \tag{21}$$

$$\begin{aligned} P_{ij}^{NL} &= (\frac{1}{2}\lambda \partial_l u_k \partial_l u_k + \mathcal{C}\partial_k u_k \partial_l u_l)\delta_{ij} + \mathcal{B}\partial_k u_k \partial_j u_i + \frac{1}{4}\mathcal{A}\partial_k u_i \partial_j u_k \\ &+ \frac{1}{2}\mathcal{B}(\partial_l u_k \partial_l u_k + \partial_l u_k \partial_k u_l)\delta_{ij} + (\lambda + \mathcal{B})\partial_k u_k \partial_i u_j \\ &+ (\mu + \frac{1}{4}\mathcal{A})(\partial_k u_j \partial_k u_i + \partial_j u_k \partial_i u_k + \partial_k u_j \partial_i u_i) \end{aligned} \tag{22}$$

Using this decomposition in the equations of motion (18) we get

$$\rho \ddot{u}_i - \partial_j P_{ji}^L = \partial_j P_{ji}^{NL} \tag{23}$$

with

$$\partial_j P_{ji}^L = \lambda \partial_i \partial_k u_k \delta_{ij} + \mu(\partial_j \partial_j u_i + \partial_j \partial_i u_j) \tag{24}$$

$$\begin{aligned} \partial_j P_{ji}^{NL} &= (\mu + \frac{1}{4}\mathcal{A})(\partial_k \partial_k u_l \partial_i u_l + \partial_k \partial_k u_l \partial_l u_i + 2\partial_l \partial_k u_i \partial_k u_l) \\ &+ (\lambda + \mu + \frac{1}{4}\mathcal{A} + \mathcal{B})(\partial_k \partial_i u_l \partial_k u_l + \partial_k \partial_l u_k \partial_l u_i) \\ &+ (\lambda + \mathcal{B})(\partial_k \partial_k u_i \partial_l u_l) + (\mathcal{B} + 2\mathcal{C})(\partial_k \partial_i u_k \partial_l u_l) \\ &+ (\frac{1}{4}\mathcal{A} + \mathcal{B})(\partial_k \partial_l u_k \partial_i u_l + \partial_k \partial_i u_l \partial_l u_k) \end{aligned} \tag{25}$$

2.2.2 Perturbation Method

Finding a solution to the nonlinear equations of motion (23) and the applicable boundary conditions represents a nonlinear boundary value problem (BVP). Since we are interested in the second-order approximation of the solution the total displacement field can be written as

$$\mathbf{u} = \mathbf{u}^{(1)} + \mathbf{u}^{(2)} \tag{26}$$

We call $\mathbf{u}^{(1)}$ the primary solution and $\mathbf{u}^{(2)}$ the secondary solution. Research and experiments on the generation of second harmonic waves suggest that the amplitude of the generated second harmonic wave is much smaller than the amplitude of the primary wave. Works like [22] show that the second harmonic wave field is commonly in the range of a hundredth of the amplitude of the primary wave field. Furthermore, this assumption is verified later in the evaluation of the solution. This suggests that

$$|\mathbf{u}^{(2)}| \ll |\mathbf{u}^{(1)}| \tag{27}$$

holds and $\mathbf{u}^{(2)}$ is only a small correction term to the dominant solution $\mathbf{u}^{(1)}$. Therefore, the BVP meets the requirement for the perturbation method (compare [3]), which is also called the perturbation condition.

Applying the perturbation method (26) to the equations of motion (23) we get

$$\rho\ddot{u}_i^{(1)} + \rho\ddot{u}_i^{(2)} - \partial_j P_{ji}^L(u_i^{(1)}) - \partial_j P_{ji}^L(u_i^{(2)}) = \partial_j P_{ji}^{NL}(u_i^{(1)} + u_i^{(2)}) \tag{28}$$

Due to the perturbation condition, the terms in $\mathbf{u}^{(2)} \cdot \mathbf{u}^{(1)}$ and $\mathbf{u}^{(2)} \cdot \mathbf{u}^{(2)}$ on the right hand side can be neglected. By decomposition one obtains

$$\rho\ddot{u}_i^{(1)} - \partial_j P_{ji}^L(u_i^{(1)}) = 0 \tag{29}$$

$$\rho\ddot{u}_i^{(2)} - \partial_j P_{ji}^L(u_i^{(2)}) = \partial_j P_{ji}^{NL}(u_i^{(1)}) \tag{30}$$

Here, Equations (29) represent a linear homogenous BVP which can be solved for $\mathbf{u}^{(1)}$. Consequently, the forcing term on the right hand sight of Equation (30) can be computed from the solution of Equation (29) and the second BVP can be solved for $\mathbf{u}^{(2)}$.

Since the curl of a P-wave field and the divergence of a S-wave field are equal to zero, Equations (29) and (30) can be written in terms of the displacement u_i

$$\ddot{u}_i^{(1)} - c_0^2 \partial_k \partial_k u_i^{(1)} = 0 \tag{31}$$

$$\ddot{u}_i^{(2)} - c_0^2 \partial_k \partial_k u_i^{(2)} = \frac{1}{\rho} \partial_j P_{ji}^{NL}(u_i^{(1)}) \tag{32}$$

with $c_0 = c_p = \sqrt{\frac{\lambda+2\mu}{\rho}}$ for P-waves and $c_0 = c_s = \sqrt{\frac{\mu}{\rho}}$ for S-waves.

We have to keep in mind that the perturbation method only yields an approximate solution and the perturbation condition must always be verified. The accuracy of the solution is dependent on the relative size of the second harmonic amplitude and therefore, it is dependent on voltage and propagation distance.

The applied approach of solving the nonlinear equations of motion is summarized and illustrated in Figure 2.2.

2.2.3 Bulk interaction of elastic waves

In order to determine the forcing term on the right hand side of Equation (30) the bulk interaction of elastic waves has to be evaluated. In nonlinear material, second harmonics are generated by two types of wave interactions: self-interaction, when a wave interacts with itself, and cross-interaction, when different waves interact with each other [5, 21].

Consider two primary waves $\mathbf{u}_{\mathrm{I}}^{(1)}$ and $\mathbf{u}_{\mathrm{II}}^{(1)}$ denoted by

$$\mathbf{u}_{\mathrm{I}}^{(1)} = A_{\mathrm{I}} \mathbf{d}_{\mathrm{I}} e^{j(\omega t - \mathbf{k}_{\mathrm{I}} \cdot \mathbf{x})} \tag{33}$$

$$\mathbf{u}_{\mathrm{II}}^{(1)} = A_{\mathrm{II}} \mathbf{d}_{\mathrm{II}} e^{j(\omega t - \mathbf{k}_{\mathrm{II}} \cdot \mathbf{x})} \tag{34}$$

where A_{I} and A_{II} are the amplitudes, $\mathbf{d}_{\mathrm{I}}$ and $\mathbf{d}_{\mathrm{II}}$ are the unit displacement vectors and $\mathbf{k}_{\mathrm{I}}$ and $\mathbf{k}_{\mathrm{II}}$ are the wave vectors. Since we are interested in the harmonics of the generated wave, we neglect the time independent term. Therefore, the forcing term can generally be written as

$$\frac{1}{\rho} \partial_j P_{ji}^{NL}(u_i^{(1)}) = \beta^{bulk} A_{\mathrm{I}} A_{\mathrm{II}} e^{j(2\omega t - \mathbf{k} \cdot \mathbf{x})} d_i \tag{35}$$

with the resulting wave vector $\mathbf{k}$ and the introduction of the nonlinearity parameter β^{bulk} according to [5].

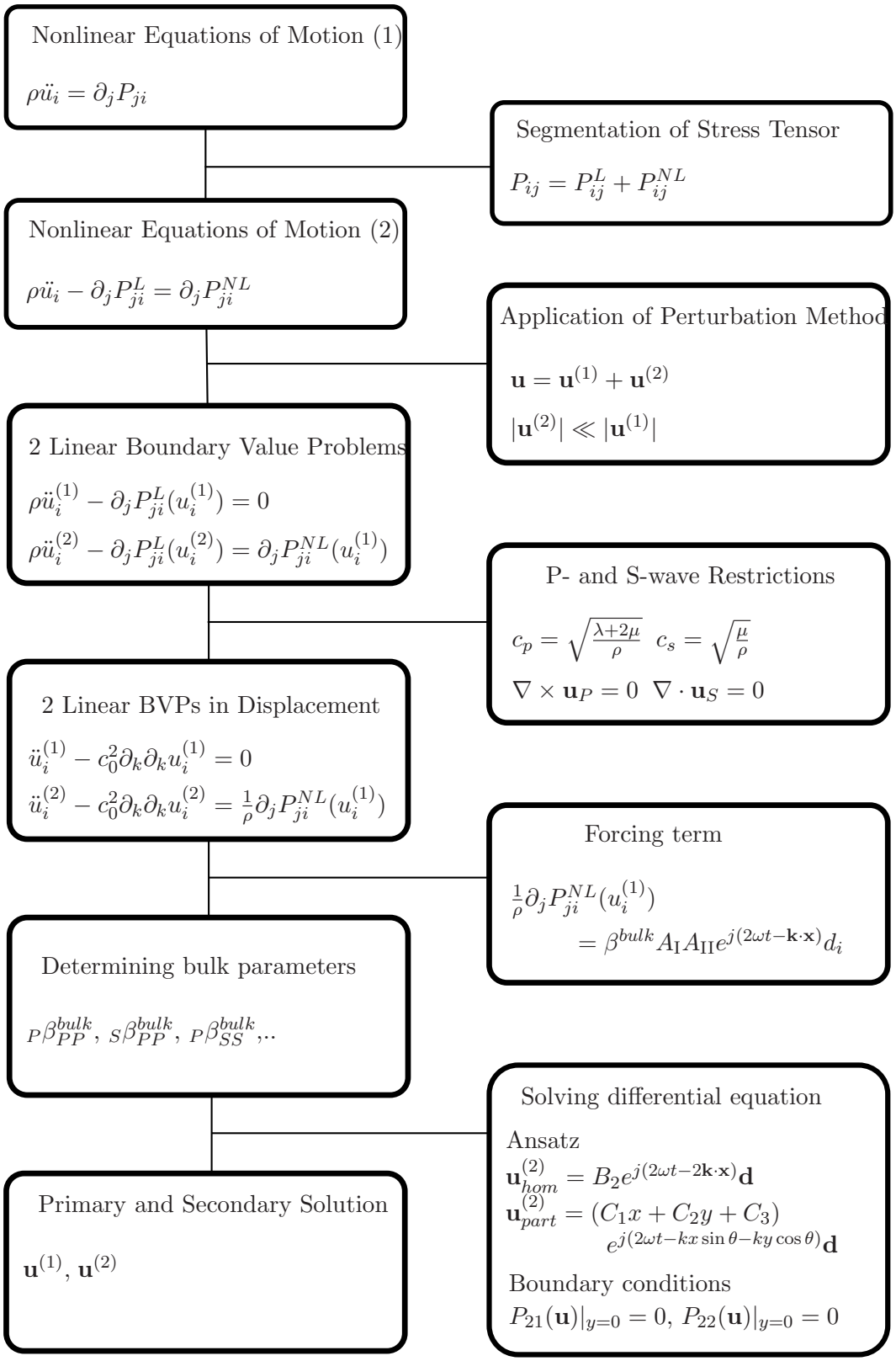

Figure 2.2: Solution procedure for solving the nonlinear equations of motion (adapted from [4])

In the case of self-interaction only a single wave interacts with itself $\mathbf{u}^{(1)} = \mathbf{u}_{\mathrm{I}}^{(1)} = \mathbf{u}_{\mathrm{II}}^{(1)}$. Using $\mathbf{u}^{(1)}$ in Equation (19) we get

$$\begin{aligned}\partial_j P_{ji}^{NL}(u_i^{(1)}) = j\Bigg(&\left(\lambda + 2\mu + \frac{\mathcal{A}}{2} + \mathcal{B}\right)(A_{\mathrm{I}} \cdot A_{\mathrm{I}})(\mathbf{k}_{\mathrm{I}} \cdot \mathbf{k}_{\mathrm{I}})\mathbf{k}_{\mathrm{I}} \\ &+ (2\lambda + 4\mu + \mathcal{A} + 2\mathcal{B})(A_{\mathrm{I}} \cdot \mathbf{k}_{\mathrm{I}})(\mathbf{k}_{\mathrm{I}} \cdot \mathbf{k}_{\mathrm{I}})A_{\mathrm{I}} \\ &+ \left(\frac{\mathcal{A}}{2} + 3\mathcal{B} + 2\mathcal{C}\right)(A_{\mathrm{I}} \cdot \mathbf{k}_{\mathrm{I}})(A_{\mathrm{I}} \cdot \mathbf{k}_{\mathrm{I}})\mathbf{k}_{\mathrm{I}}\Bigg)\frac{1}{2}e^{j(2\omega t - 2\mathbf{k}_{\mathrm{I}} \cdot \mathbf{x})}\end{aligned} \tag{36}$$

with the resulting wave vector $\mathbf{k} = 2\mathbf{k}_{\mathrm{I}}$. Using this result in Equation (35) for P-waves and for S-waves we get

$$_P\beta_{PP}^{bulk} = \frac{jk_p^3}{2\rho}(3\lambda + 6\mu + 2\mathcal{A} + 6\mathcal{B} + 2\mathcal{C}) \tag{37}$$

$$_S\beta_{PP}^{bulk} = 0 \tag{38}$$

$$_P\beta_{SS}^{bulk} = \frac{jk_s^3}{2\rho}(\lambda + 2\mu + \frac{\mathcal{A}}{2} + \mathcal{B}) \tag{39}$$

$$_S\beta_{SS}^{bulk} = 0 \tag{40}$$

Note that $_P\beta_{PP}^{bulk} =_P \beta_{P_iP_i}^{bulk} =_P \beta_{P_rP_r}^{bulk}$ and $_P\beta_{SS}^{bulk} =_P \beta_{S_iS_i}^{bulk} =_P \beta_{S_rS_r}^{bulk}$.

Proceeding similarly for the interaction of two different types of waves one gets the remaining nonlinearity parameters β^{bulk}. There is only one special case where cross interaction has a noticeable impact on the generation of the second harmonic. This case is further explained in Section 3.2. In most cases only the self-interaction results in a resonant case and is therefore significant for measurements. Consequently, this thesis concentrates on the case of self interaction. For further reading for the case of cross interaction the reader is referred to the works of [5, 21].

2.2.4 Solution of the Equation of Motion

Note that in the mathematical analysis we assume our medium to be infinitely extended in x- and z-direction. Without loss of generality we let the wave normal lie in the x,y-plane as illustrated in Figure 2.3. Therefore, the displacement field lies in the x,y-plane. Restricting this case to in-plane motion reduces the problem to two dimensions. With the results presented above a solution to the equations of motion is derived in this chapter.

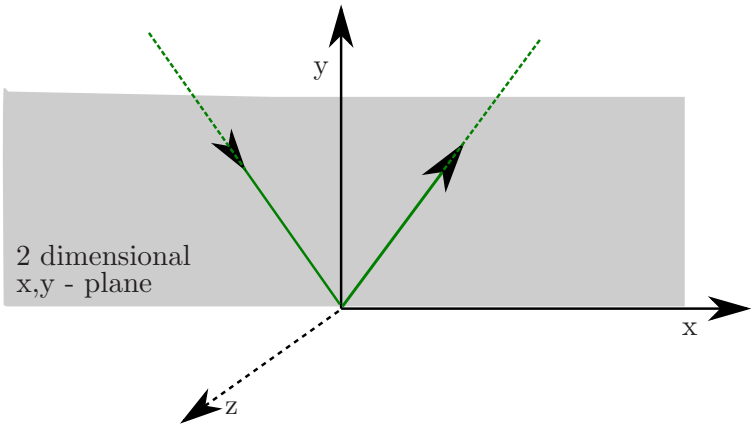

Figure 2.3: Coordinate system of the infinite half-space

Then the unspecified constants are determined in the next chapter for distinct problems. Plugging in the forcing term of Equation (35) into the BVP we get

$$\ddot{u}_i^{(1)} - c_0^2 \partial_k \partial_k u_i^{(1)} = 0 \tag{41}$$

$$\ddot{u}_i^{(2)} - c_0^2 \partial_k \partial_k u_i^{(2)} = \beta^{bulk} A_{\mathrm{I}} A_{\mathrm{II}} e^{j(2\omega t - \mathbf{k}\cdot\mathbf{x})} d_i \tag{42}$$

The solution to Equation (31) is

$$\mathbf{u}^{(1)} = B_1 e^{j(\omega t - \mathbf{k}\cdot\mathbf{x})} \mathbf{d} \tag{43}$$

with B_1 being an undetermined constant. Similarly, the homogeneous solution to Equation(32) is

$$\mathbf{u}_{hom}^{(2)} = B_2 e^{j(2\omega t - 2\mathbf{k}\cdot\mathbf{x})} \mathbf{d} \tag{44}$$

with the undetermined constant B_2. For the particular solution to Equation (32) we use the ansatz

$$\mathbf{u}_{part}^{(2)} = (C_1 x + C_2 y + C_3) e^{j(2\omega t - kx\sin\theta - ky\cos\theta)} \mathbf{d} \tag{45}$$

that gives us following equation when plugged into Equation (32)

$$(-4\omega^2 + c_0^2 k^2)(C_1 x + C_2 y + C_3) + 2jc_0^2 k C_1 \sin\theta + 2jc_0^2 k C_2 \cos\theta = \beta^{bulk} A_{\mathrm{I}} A_{\mathrm{II}} \tag{46}$$

Since the right hand side does not contain any terms of x or y, those terms with x- or y-dependence must vanish on the left hand side as well. Therefore, we get two cases, the resonant case where $k = 2k_0$ and the non resonant case where $C_1 = C_2 = 0$. As stated

before, we are especially interested in the resonant case. This is the measurable part in a general application as the amplitude of the non resonant solution is not growing with propagation distance.

For further information the reader is referred to [4]. As C_1 and C_2 are related and can be expressed by the introduction of the constant α^{surf}, the resonant particular solution can be written as

$$\mathbf{u}^{(2)}_{part} = \left(\frac{A_{\mathrm{I}} A_{\mathrm{II}}}{4jk_0c_0^2} \left(\alpha^{surf} \sin\theta x + \left(\frac{\beta^{bulk} - \alpha^{surf} \sin^2\theta}{\cos\theta} \right) y \right) + C_3 \right) e^{j(2\omega t - 2k_0 x \sin\theta - 2k_0 y \cos\theta)} \mathbf{d} \tag{47}$$

Adding the homogeneous and the particular solution we finally get the complete solution for Equation (32)

$$\begin{aligned} \mathbf{u}^{(2)} = & \left(\frac{A_{\mathrm{I}} A_{\mathrm{II}}}{4jk_0c_0^2} \left(\alpha^{surf} \sin\theta x + \left(\frac{\beta^{bulk} - \alpha^{surf} \sin^2\theta}{\cos\theta} \right) y \right) + \gamma^{surf} \right) \\ & \cdot e^{j(2\omega t - 2k_0 x \sin\theta - 2k_0 y \cos\theta)} \mathbf{d} \end{aligned} \tag{48}$$

where $\gamma^{surf} = B_2 + C_3$. Note that this solution still has two unknown constants α^{surf} and γ^{surf} that must be determined by evaluating the boundary conditions.

2.2.5 Boundary Conditions

In case of a stress-free surface the boundary condition expressed by the Piola-Kirchhoff stress tensor are given by

$$P_{21}|_{y=0} \stackrel{!}{=} 0 \;\text{ and }\; P_{22}|_{y=0} \stackrel{!}{=} 0 \tag{49}$$

Using the perturbation method and the perturbation condition we obtain

$$P_{21}(\mathbf{u}^{(1)} + \mathbf{u}^{(2)})|_{y=0} = P^L_{21}(\mathbf{u}^{(1)})|_{y=0} + P^{NL}_{21}(\mathbf{u}^{(1)})|_{y=0} + P^L_{21}(\mathbf{u}^{(2)})|_{y=0} \tag{50}$$

$$P_{22}(\mathbf{u}^{(1)} + \mathbf{u}^{(2)})|_{y=0} = P^L_{22}(\mathbf{u}^{(1)})|_{y=0} + P^{NL}_{22}(\mathbf{u}^{(1)})|_{y=0} + P^L_{22}(\mathbf{u}^{(2)})|_{y=0} \tag{51}$$

Since the linear stresses in $\mathbf{u}^{(1)}$ satisfy the linear boundary condition $P^L_{21}(\mathbf{u}^{(1)})|_{y=0} = \sigma_{21}(\mathbf{u}^{(1)})|_{y=0} = 0$ and $P^L_{22}(\mathbf{u}^{(1)})|_{y=0} = \sigma_{22}(\mathbf{u}^{(1)})|_{y=0} = 0$ we finally get the following boundary conditions

$$P^{NL}_{21}(\mathbf{u}^{(1)})|_{y=0} = -P^L_{21}(\mathbf{u}^{(2)})|_{y=0} \tag{52}$$

$$P^{NL}_{22}(\mathbf{u}^{(1)})|_{y=0} = -P^L_{22}(\mathbf{u}^{(2)})|_{y=0} \tag{53}$$

CHAPTER III

SECOND HARMONIC GENERATION AT A FREE BOUNDARY

With the theoretical background derived in Chapter 2 we can now evaluate the second harmonic generation at a stress-free boundary. A distinct model to be analyzed is illustrated in Figure 3.1. This model is derived from a possible measurement setup which is then used in the simulations and in the experiment. The gray area illustrates the wedge on which the transducer is be glued to. The wedge enables omitting waves at an oblique angle into the specimen. The white area is the specimen which shall be investigated. In the following, Figure 3.1 is further explained.

3.1 Primary wave field

As shown in Figure 3.1, the transducer generates a P-wave which is then transmitted and reflected at the interface of the wedge and the specimen. At the solid-solid interface the generated P-wave causes a transmitted S-wave and a transmitted P-wave propagating at different angles into the specimen, as explained in Section 2.1.3. Note that the reflected waves at the solid-solid interface of wedge and specimen are not drawn in Figure 3.1 as they are not of interest in the following analysis.

The transmitted S-wave is reflected at bottom surface position 1, causing a reflected P-wave and a reflected S-wave. The transmitted P-wave is reflected at bottom surface position 2 and causes another reflected P-wave and another reflected S-wave. In the following, the position where the reflected S-wave arrives is referred to as position 3. The position where the mode-converted reflected S-wave as well as the mode-converted reflected P-wave arrive is referred to as position 4, and the position where the reflected P-wave arrives is referred to as position 5, shown in Figure 3.1. Especially position 4 and position 5 turn out to be possible receiver positions.

Thereby, the incident angle of the generated incident P-wave is a variable parameter. Since we want to evaluate the reflected P- and S-wave, we only consider incident P-wave

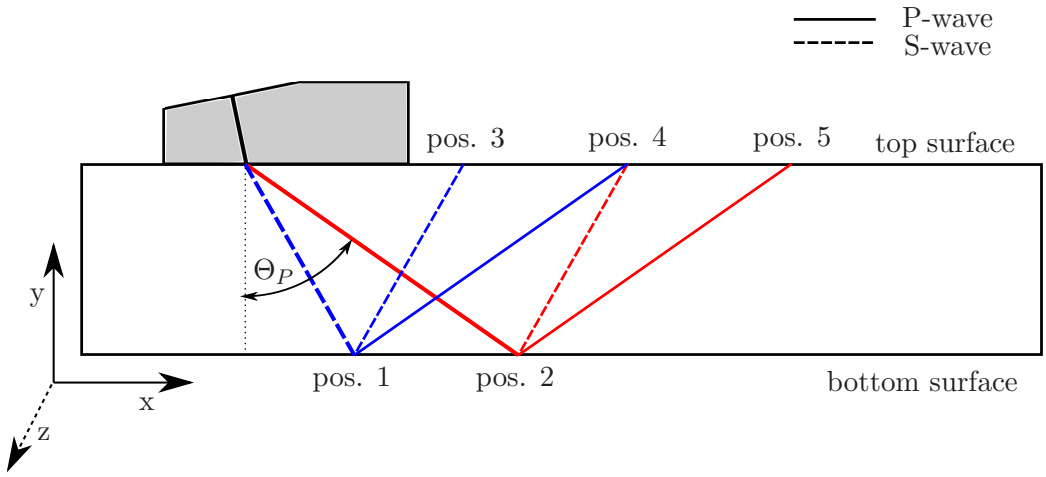

Figure 3.1: Investigated setup with reflection of an initial P- and S-wave at a stress-free boundary

Table 3.1: Material properties of Acrylic Plastic

Description	Symbol	**Value**
Young's modulus	E	3.2 GPa
Poisson's ratio	ν	0.35
mass density	ρ	1190 kg/m^3
Lamé parameter[a]	λ	2.8 GPa
Lamé parameter[a]	μ	1.2 GPa
velocity P-wave[a]	c_{P1}	2077.5 m/s
velocity S-wave[a]	c_{S1}	998.0 m/s

[a]Calculated from listed properties

angles up to the critical angle $\Theta_{cr} = \sin^{-1}(c_{P1}/c_{P2})$.

In order to evaluate this model we have to use material properties. According to several experimental works (e.g. [18, 27]) the wedge is chosen to be out of Acrylic Plastic. The corresponding relevant properties of the material are listed in Table 3.1. These values are taken from the material library of COMSOL. The material of the specimen is chosen to be aluminum. Aluminum has been of interest in various works (e.g. [29, 30]), it has a wide application area and the material properties are well-investigated. Again, we use the properties of generic aluminum available from the material library of COMSOL. The relevant material properties are listed in Table 3.2.

Applying these material properties, the primary wave field can be evaluated. The normalized amplitudes of the reflected and transmitted S-wave and P-wave for the angles

Table 3.2: Material properties of Aluminum

Description	Symbol	**Value**
Young's modulus	E	70 GPa
Poisson's ratio	ν	0.33
mass density	ρ	2700 kg/m^3
Lam*é* parameter	λ	51 GPa
Lam*é* parameter	μ	26 GPa
TOEC	$\mathcal{A}$	-350 GPa
TOEC	$\mathcal{B}$	-155 GPa
TOEC	$\mathcal{C}$	-95 GPa
velocity P-wave[a]	c_{P2}	6176.4 m/s
velocity S-wave[a]	c_{S2}	3103.2 m/s

[a]Calculated from listed properties

$0 < \Theta_i < \Theta_{cr} \approx 19.5°$ are shown in Figure 3.2. This correlates with $0 < \Theta_P < 90°$. Since the incident angle of interest is in a small range and not very descriptive, the reference angle is chosen to be Θ_P in this thesis. Θ_P is the angle of the transmitted P-wave in the specimen, as illustrated in Figure 3.1. Note that by knowing Θ_P, the incident angle Θ_i can easily and uniquely be determined.

As shown in Figure 3.2, it is necessary to evaluate both P-wave as well as S-wave at the stress-free boundary. The amplitudes of the reflected primary wave fields of the P-wave and the S-wave with respect to the generated amplitude for different angles Θ_P are shown in Figure 3.3. There are four primary waves arriving at the surface, that have to be taken into consideration: P- and S-wave reflected from the transmitted P-wave, and P- and S-wave reflected from the transmitted S-wave.

3.2 Secondary wave field

In order to evaluate the secondary field the transmitted P- and S-wave are analyzed separately on the basis of the mathematical approach explained in Section 2.2.

3.2.1 Transmitted P-wave

In this section the secondary wave field caused by the transmitted P-wave at the presence of a stress-free boundary is evaluated. The transmitted S-wave is not considered in this section.

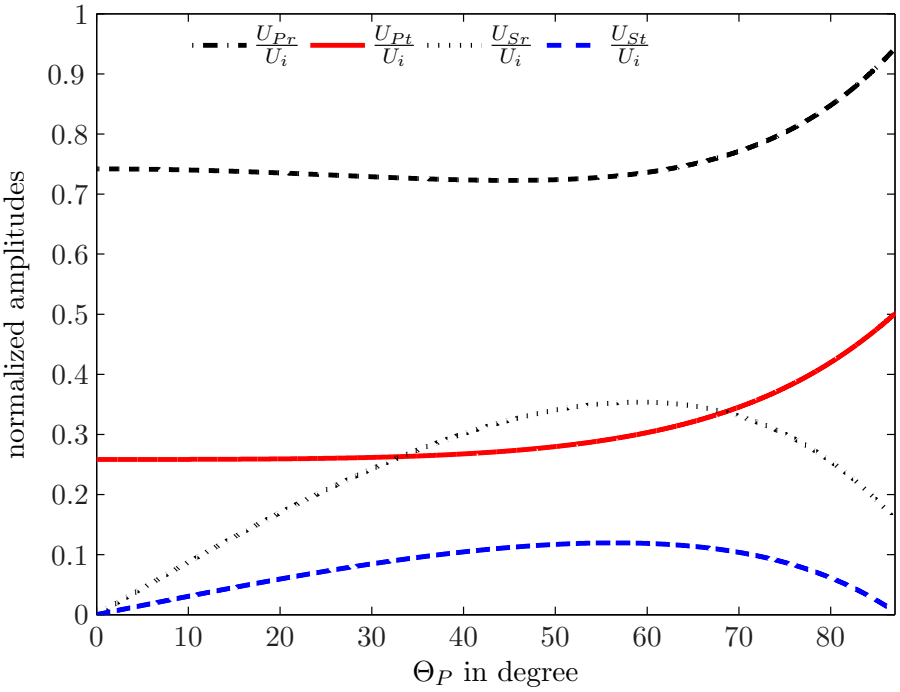

Figure 3.2: Normalized amplitude of transmitted and reflected waves

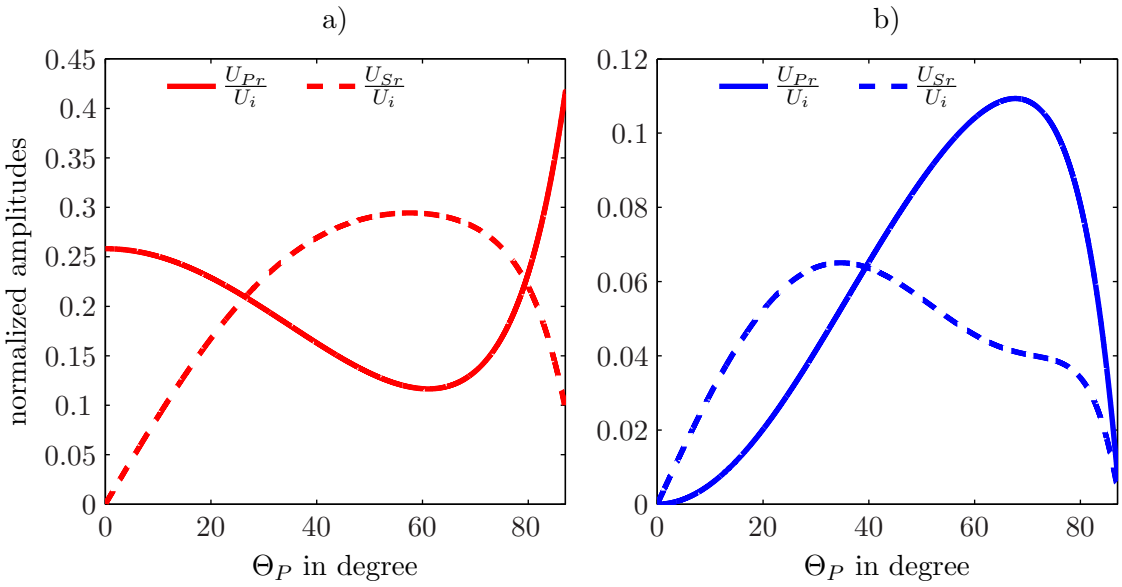

Figure 3.3: Amplitudes of the reflected primary waves of the a) transmitted P-wave and b) transmitted S-wave normalized by the generated amplitude A_i plotted over the different angles Θ_P

Table 3.3: Summary of the secondary wave field considering only the transmitted P-wave adapted from [4]

Wave	Interaction	Generated by	Wave number	Angle	Resonance
${}_P\mathbf{u}^{(2)}_{PtPt}$	Self	$\mathbf{u}^{(1)}_{Pt}$	$2k_P$	Θ_P	Yes
${}_P\mathbf{u}^{(2)}_{PtPr}$	Cross	$\mathbf{u}^{(1)}_{Pt}$, $\mathbf{u}^{(1)}_{Pr}$	$k_{PtPr} = 2k_P \sin\Theta_P$	$90°$	No
${}_P\mathbf{u}^{(2)}_{PtSr}$	Cross	$\mathbf{u}^{(1)}_{Pt}$, $\mathbf{u}^{(1)}_{Sr}$	$k_{PtSr} = 2k_P \frac{\sin\Theta_P}{\sin\Psi}$	Ψ	only for $\Theta_P = \Theta^*_P$
${}_S\mathbf{u}^{(2)}_{PtSr}$	Cross	$\mathbf{u}^{(1)}_{Pt}$, $\mathbf{u}^{(1)}_{Sr}$	$k_{PtSr} = 2k_P \frac{\sin\Theta_P}{\sin\Psi}$	Ψ	No
${}_P\mathbf{u}^{(2)}_{PrPr}$	Self	$\mathbf{u}^{(1)}_{Pr}$	$2k_P$	Θ_P	Yes
${}_P\mathbf{u}^{(2)}_{PrSr}$	Cross	$\mathbf{u}^{(1)}_{Pr}$, $\mathbf{u}^{(1)}_{Sr}$	$k_{PrSr} = 2k_P \frac{\sin\Theta_P}{\sin\Phi}$	Φ	No
${}_S\mathbf{u}^{(2)}_{PrSr}$	Cross	$\mathbf{u}^{(1)}_{Pr}$, $\mathbf{u}^{(1)}_{Sr}$	$k_{PrSr} = 2k_P \frac{\sin\Theta_P}{\sin\Phi}$	Φ	No
${}_P\mathbf{u}^{(2)}_{SrSr}$	Self	$\mathbf{u}^{(1)}_{Sr}$	$2k_S$	Θ_S	No
${}_S\mathbf{u}^{(2)}_{SrSr}$	Self	$\mathbf{u}^{(1)}_{Sr}$	$2k_S$	Θ_S	Yes

with $\Psi = \arctan \frac{2k_P \sin\Theta_P}{k_S \cos\Theta_S - k_P \cos\Theta_P}$, $\Phi = \arctan \frac{2k_P \sin\Theta_P}{k_S \cos\Theta_S + k_P \cos\Theta_P}$

According to the perturbation method, the secondary wave field generated by the transmitted P-wave under the presence of a stress-free boundary can be determined by considering all self- and cross-interactions of the primary waves. Therefore, the resulting complete expression for the secondary field is following

$$\begin{aligned}\mathbf{u}^{(2)} = {}_P\mathbf{u}^{(2)}_{PtPt} + {}_P\mathbf{u}^{(2)}_{PtPr} + {}_P\mathbf{u}^{(2)}_{PtSr} + {}_S\mathbf{u}^{(2)}_{PtSr} + {}_P\mathbf{u}^{(2)}_{PrPr} \\ + {}_P\mathbf{u}^{(2)}_{PrSr} + {}_S\mathbf{u}^{(2)}_{PrSr} + {}_S\mathbf{u}^{(2)}_{SrSr} + {}_P\mathbf{u}^{(2)}_{SrSr}\end{aligned} \tag{54}$$

where the notation is adapted from [4] in order to uniquely address all waves. Thereby, the prefixed index expresses the nature of the wave itself and the suffixed index expresses the origin of the wave cause, the two primary waves that interact. The term ${}_P\mathbf{u}^{(2)}_{PtPr}$ for example represents a second harmonic P-wave that results by the cross-interaction of the transmitted P-wave A_{Pt} and the reflected P-wave A_{Pr}. For further explanation of the second harmonic wave field generated by interaction the reader is referred to [5] and [21]. A summary of the results is presented in Table 3.3 adapted from [5]. Since we want to evaluate the method generally at an oblique angle, we only consider the general case where $\Theta_P \neq \Theta^*_P$, with Θ^*_P being the only angle where ${}_P\mathbf{u}^{(2)}_{PtSr}$ shows resonance. This results in only three not negligible terms, the resonant cases ${}_P\mathbf{u}^{(2)}_{PtPt}$, ${}_P\mathbf{u}^{(2)}_{PrPr}$ and ${}_S\mathbf{u}^{(2)}_{SrSr}$. These

Table 3.4: Summary of the secondary wave field considering only the transmitted S-wave adapted from [4]

Wave	Interaction	Generated by	Wave number	Angle	Resonance
${}_P\mathbf{u}^{(2)}_{StSt}$	Self	$\mathbf{u}^{(1)}_{St}$	$2k_S$	Θ_S	No
${}_P\mathbf{u}^{(2)}_{StSr}$	Cross	$\mathbf{u}^{(1)}_{St}$, $\mathbf{u}^{(1)}_{Sr}$	$k_{StSr} = 2k_S \sin\Theta_S$	$90°$	No
${}_P\mathbf{u}^{(2)}_{PrPr}$	Self	$\mathbf{u}^{(1)}_{Pr}$	$2k_P$	Θ_P	Yes
${}_P\mathbf{u}^{(2)}_{PrSr}$	Cross	$\mathbf{u}^{(1)}_{Pr}$, $\mathbf{u}^{(1)}_{Sr}$	k_{PrSr}	Φ	No
${}_S\mathbf{u}^{(2)}_{PrSr}$	Cross	$\mathbf{u}^{(1)}_{Pr}$, $\mathbf{u}^{(1)}_{Sr}$	k_{PrSr}	Φ	No
${}_P\mathbf{u}^{(2)}_{SrSr}$	Self	$\mathbf{u}^{(1)}_{Sr}$	$2k_S$	Θ_S	No
${}_S\mathbf{u}^{(2)}_{SrSr}$	Self	$\mathbf{u}^{(1)}_{Sr}$	$2k_S$	Θ_S	Yes

with $k_{PrSr} = \sqrt{(2k_P \sin\Theta_P)^2 + (k_S \cos\Theta_S + k_P \cos\Theta_P)^2}$, $\Phi = \arctan \frac{2k_S \sin\Theta_S}{k_S \cos\Theta_S + k_P \cos\Theta_P}$

waves are of particular interest as their amplitudes depend on the propagation distance. Those three waves are further investigated.

3.2.2 Transmitted S-wave

Similar to the consideration of the P-wave, the S-wave can be analyzed. The resulting complete expression for the secondary wave field is following, where each term is further explained in Table 3.4 adapted from [4].

$$\begin{aligned}\mathbf{u}^{(2)} = {}_P\mathbf{u}^{(2)}_{StSt} + {}_P\mathbf{u}^{(2)}_{StSr} + {}_P\mathbf{u}^{(2)}_{PrPr} + {}_P\mathbf{u}^{(2)}_{PrSr} \\ + {}_S\mathbf{u}^{(2)}_{PrSr} + {}_P\mathbf{u}^{(2)}_{SrSr} + {}_S\mathbf{u}^{(2)}_{SrSr}\end{aligned} \tag{55}$$

3.3 Model analysis for different parameters

Putting these results together, the second harmonic wave field for the setup in Figure 3.1 can be evaluated. The result is illustrated in Figure 3.4 for different angles of the transmitted P-wave. The thickness of the specimen is chosen to be 0.025 m and the amplitude of the transducer is $15 \cdot 10^{-10}$ m. Those values are also analyzed in the simulations in Chapter 4. Note that the second harmonic wave field is plotted over the x-axis of the model. To illustrate positions 1 and 2 at the bottom surface and position 3, 4 and 5 at the top surface the reader is referred to Figure 3.1. In order to improve the readability of the figures the

horizontal and vertical scales vary for different angles. In Figure 3.5 a second plot is added for the angles $\Theta_P = 20°$ and $\Theta_P = 70°$ with fixed horizontal and vertical axis in order to enable comparison of these results for relative values.

There are two bottom positions marked. The first one is where the S-wave is reflected. It can be seen that there is no second harmonic wave generated by the transmitted S-wave. Due to the transmitted S-wave there is a reflected P- and S-wave. The secondary wave field generated by the reflected S-wave is negligible small. Therefore, there is no second harmonic measurable at position 3. But the second harmonic generated by the reflected P-wave is not negligible especially with increasing angle. Consequently, we have to consider the reflected P-wave caused by the transmitted S-wave while evaluating position 4.

At bottom surface position 2 the transmitted P-wave is reflected. Note that at this bottom surface position there is a measurable second harmonic wave. Both, the reflected P-wave and the reflected S-wave contribute to the second harmonic wave field. Therefore, position 4 and 5 are possible measurement points. Note that the reflected S-wave propagates with constant amplitude since there is no bulk nonlinearity for this wave. It is solely a result of the stress-free boundary.

In order to further investigate position 4 and 5, the second harmonic wave field is plotted over increasing TOECs $\mathcal{A}, \mathcal{B}, \mathcal{C}$, over different specimen thicknesses L and over a range of incident amplitudes A_i for different angles. The default values are non-increased TOECs, $L = 0.025$ m and $A_i = 15 \times 10^{-10}$ m. The results are shown in Figure 3.6 for position 5 in column a) and for position 4 in column b). Figure 3.6 illustrates the proportionality of the amplitude of the generated second harmonic A_2 to the increase factor of the TOECs and with it to the nonlinearity factor β, the thickness of the specimen L and the incident generated amplitude A_i squared

$$A_2 \propto \beta L A_1^2 \tag{56}$$

Also the plots show that generally an increase in the incident angle Θ_i and at the same time Θ_P and Θ_S leads to an increase in the amplitude of the second harmonic wave field. This is simply a result of the longer propagation distance due to larger angles. With longer propagation distances the accumulating waves can achieve higher amplitudes.

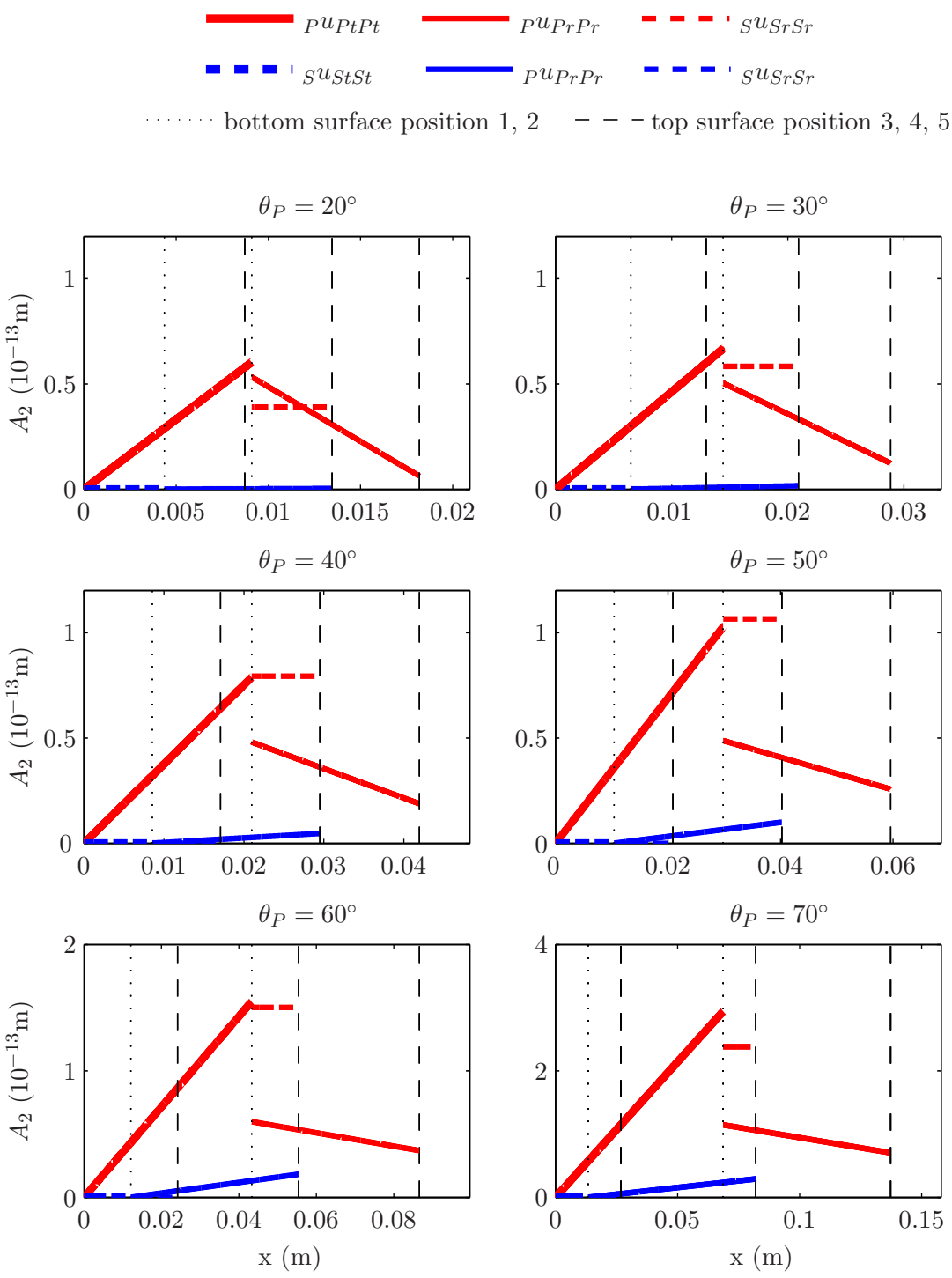

Figure 3.4: Superposition of the secondary wave field of the transmitted P- and S-wave for different angles

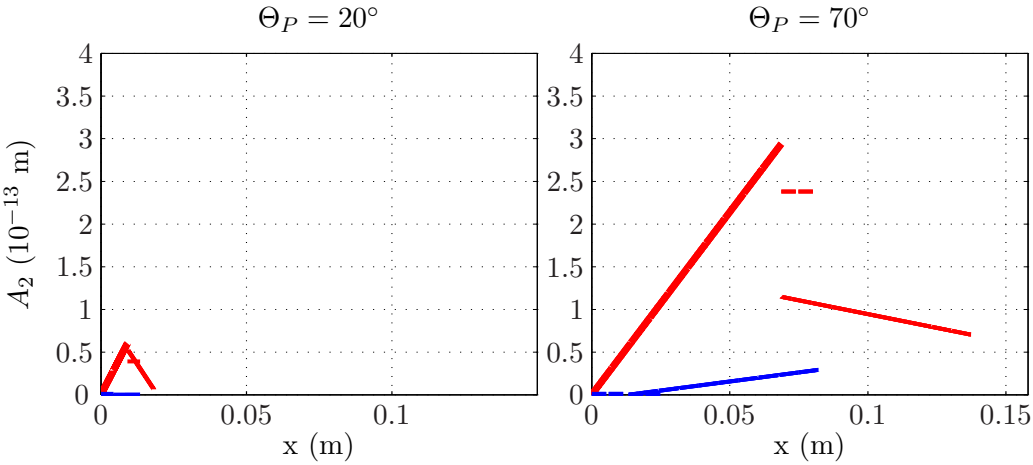

Figure 3.5: Comparison of the secondary wave field of the transmitted P- and S-wave for $\Theta_P = 20°$ and $\Theta_P = 70°$

Especially the amplitude of the second harmonic wave being proportional to the TOECs is an important feature in order to draw inferences from the second harmonic amplitude about the nonlinearity of the material. A common method to get information about the nonlinearity of a material is to measure the second harmonic amplitude A_2 versus the amplitude of the fundamental squared A_1^2 for increasing generated incident amplitude A_i [22, 26]. The slope of the linear fit of such data points represents the nonlinearity factor β^{rel}. Without having to calculate the absolute value of β, the value of the slope β^{rel} can be normalized and relatively compared. Therefore, the change in nonlinearity can be determined and conclusions about the material can be drawn. In Figure 3.7 an aluminum specimen of 0.025 m thickness is evaluated for different generated incident amplitudes $5 \times 10^{-10} < A_i < 25 \times 10^{-10}$ at an angle of $\Theta_P = 50°$. It can be seen that the amplitudes of all the arriving generated second harmonic waves are linear to the TOECs and consequently can be used for nonlinearity measurements.

As a result position 4 and 5 are potential measurement positions that have to be further investigated. Especially how the interaction of two arriving waves at position 4 influences the measurable second harmonic has to be investigated. It is important to determine whether both position 4 and 5 are possible measurement positions, and consequently, which position should be preferred in a measurement setup.

Another variable parameter is the angle. In Figure 3.8 the amplitude of the second

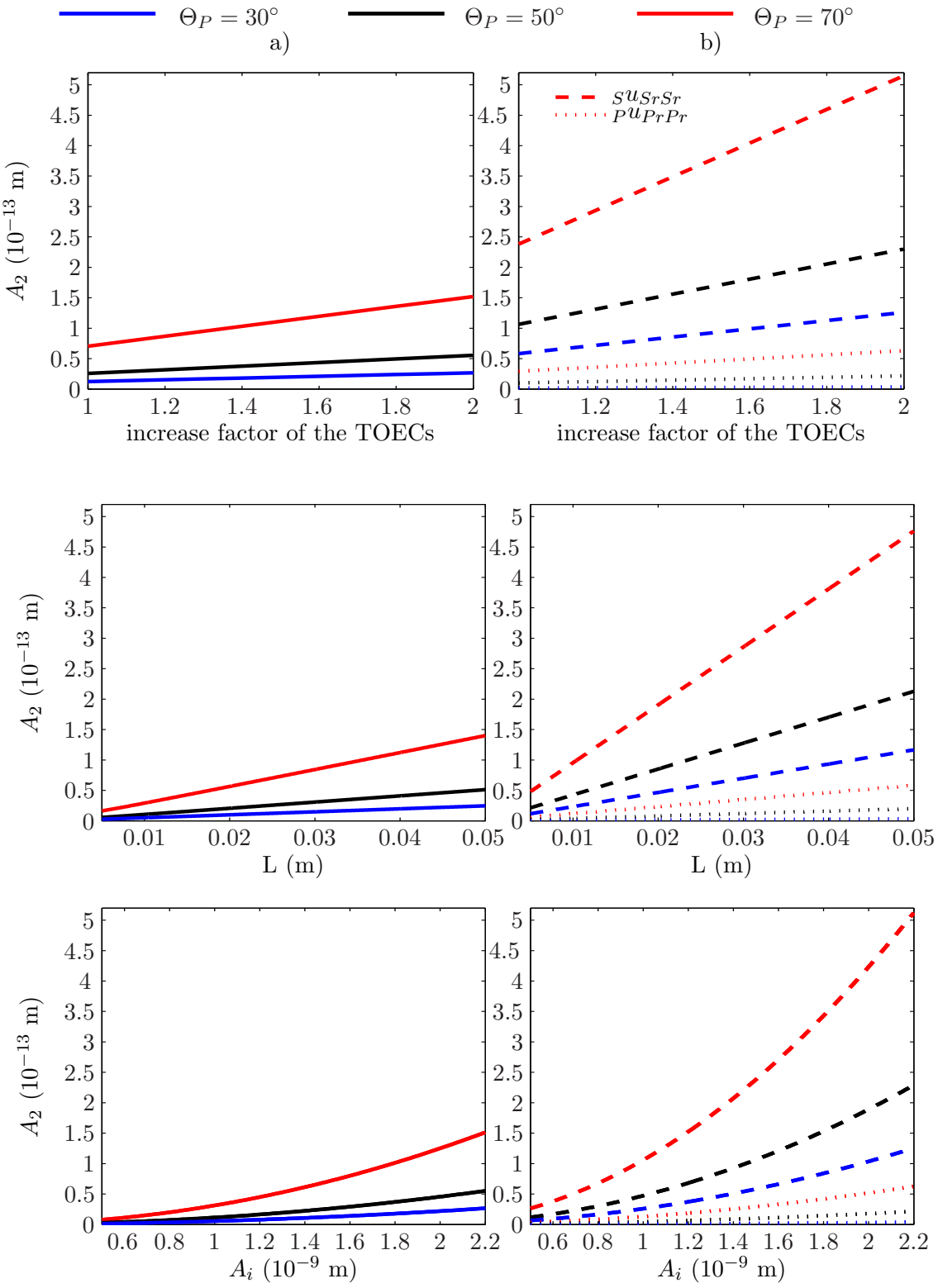

Figure 3.6: Generated second harmonic wave field plotted over different values of TOECs, thickness and generated incident amplitude for different angles a) at position 5 and b) at position 4

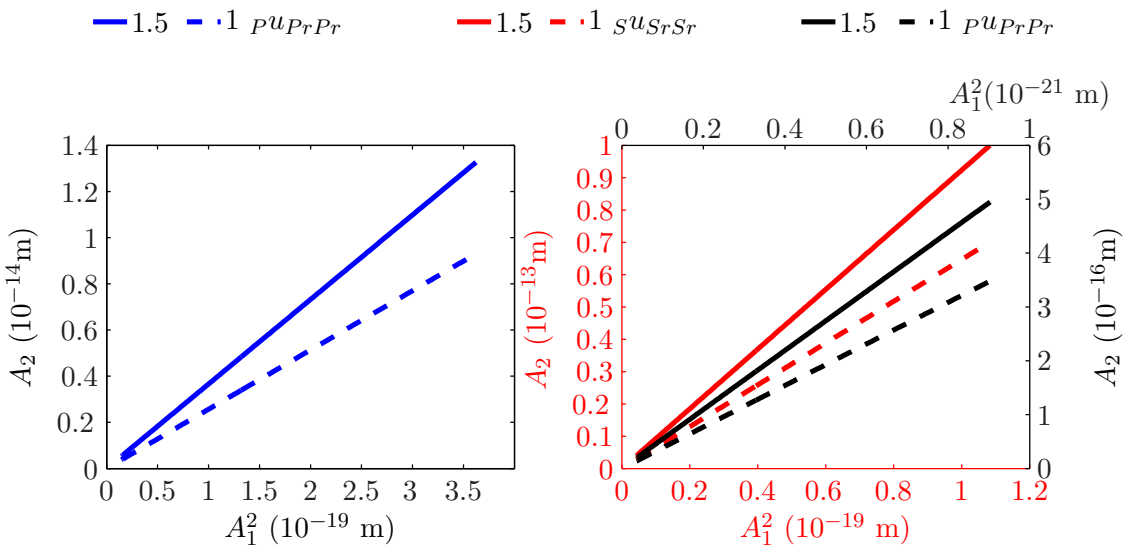

Figure 3.7: Generated second harmonic wave field plotted over arriving fundamental waves for increased TOECs a) at position 5 and b) at position 4

harmonic over different angles is illustrated. Since only the displacement perpendicular to the surface can be measured, the y-component is calculated and added to the graphic. It can be seen that for $_Pu_{PrPr}$ arriving at position 5 the increasing angle has a smaller increase in the generated second harmonic in the y-component than the increase of $_Su_{SrSr}$ arriving at position 4. The reason is that at position 5 the absolute amplitude increases due to longer propagation distances on the one hand. On the other hand, the out of plane displacement part decreases since the angle increases. At position 4 the absolute amplitude increases and the angle changes in favor of the out of plane displacement. Generally speaking, at position 4 the y-component of the second harmonic amplitude increases significantly faster with increasing angle, whereas the amplitude at position 5 only increases slightly in the range of $\Theta_P = 30°$ to $60°$. Other points to take into consideration for choosing the angle is that for small angles the possibility of unintentional interference increases due to bream spreading. Increasing angles on the other hand cause more attenuation and diffraction. Furthermore, the angle should be chosen according to the intention whether one wants to measure rather local defects or overall state of the material.

Note that in this Figure 3.8 the special angle Θ_P^*, which is the only angle where $_P\mathbf{u}_{PtSr}^{(2)}$ shows resonance, is not especially evaluated. Therefore, the values at $\Theta_P = \Theta_P^* \approx 52.5°$

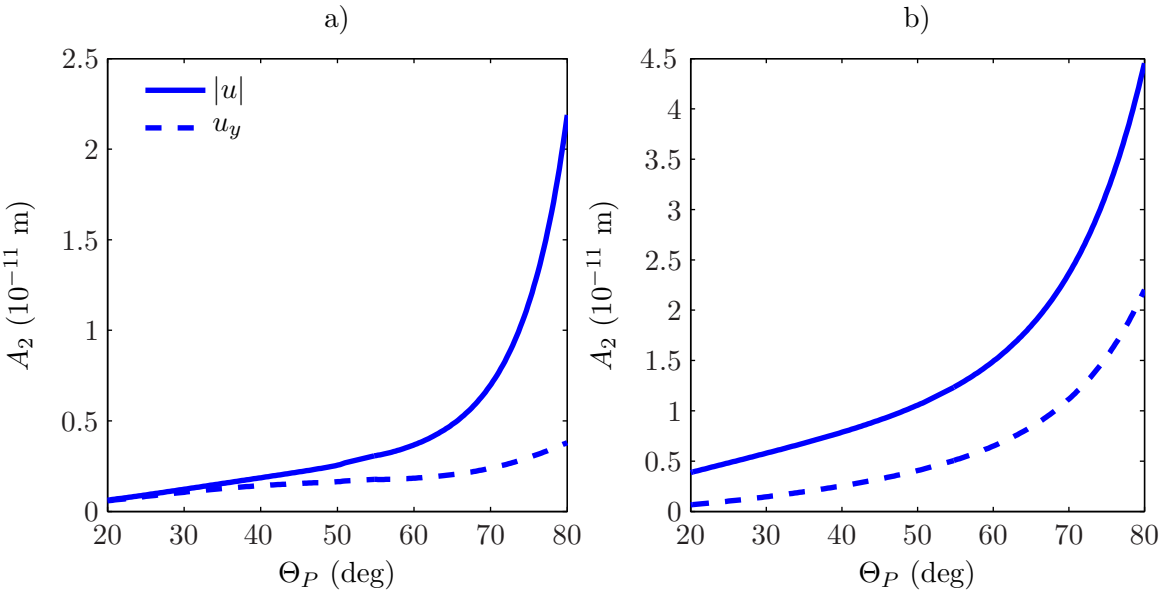

Figure 3.8: Generated second harmonic wave field over different angles Θ_P for a) ${}_Pu_{PrPr}$ arriving at position 5 and b) ${}_Su_{SrSr}$ arriving at position 4

can vary considerably.

The analytical evaluation showed that acoustic nonlinearity of a material can be measured with access to only one side of the specimen using the reflection at the stress-free boundary. The results suggest following measurement method: chose a fixed angle, increase input amplitude and measure the slope of A_2 over A_1^2 at position 4 or position 5. The slope is then proportional to the nonlinearity of the material.

In the next Chapter this measurement method is further investigated in a numerical FE simulation. The analytical results are compared to the numerical results followed by experimental measurements. Therefore, the reader has to keep in mind the limitations of the mathematical approach:

- perturbation method results in an approximate solution; perturbation condition has to be fulfilled
- for isotropic and homogenous materials
- assumption of infinite half-space
- assumption of plane waves; attenuation and diffraction not taken into account

CHAPTER IV

SIMULATIONS - FINITE ELEMENT MODEL

In the present chapter the theoretically developed model of Chapter 3 is implemented in a commercial FE code, COMSOL multiphysics 4.3b, in order to compare and validate the mathematical approach. Furthermore, the feasibility for an experimental measurement is evaluated.

In COMSOL the structural mechanics module and the nonlinear structural materials module are added to the basic modules in order to incorporate hyperelasticity and to enable the generation of higher harmonics.

The time and space dependent problem presented in this model requires careful setup of the mesh, time step, tolerance controls and other model parameters in order to reach convergence and get accurate results up to the second harmonic while not making the model computationally too expensive. The influence of mesh size and time steps in the simulation of ultrasonic wave propagation in solids is described for example in [16]. In the following section the most important aspects of the FEM simulations are presented followed by the confirmation of the model by variation of several parameters. The post processing of the data is explained and the first conclusions for eliminating unwanted influences are drawn.

4.1 Modeling

The model is chosen to mimic an experimental setup where the wave is generated at an oblique angle using a wedge transducer. The analysis is in the time domain. A sketch of the model is illustrated in Figure 4.1, which is further described in the following sections.

4.1.1 Geometry

The model consists of two parts, the wedge and the specimen. The use of a wedge enables P-waves in the specimen at arbitrary angles of incidence. This is a standard technique in NDE experiments and can therefore be the basis for further experimental investigation and

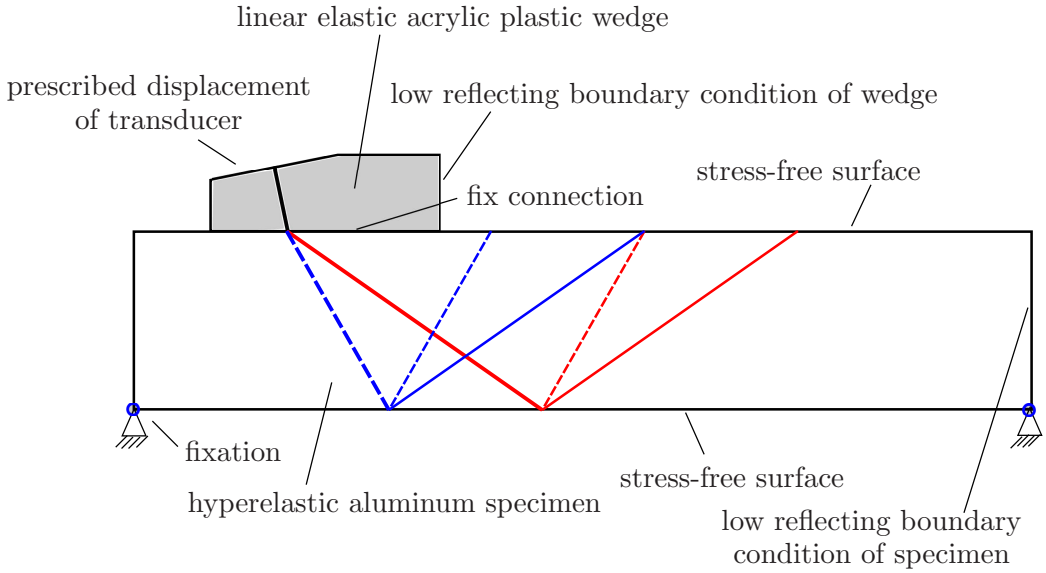

Figure 4.1: FE simulation model with material, physics and boundary conditions

comparison. The angle of the wedge is dependent on the angle the P-wave and the S-wave shall meet the stress-free boundary. Another important parameter is the length of the wedge in order to avoid surface waves. This issue is further discussed in Section 4.3.2. The specimen is 2.6 cm thick. This size is a compromise between computational expense and the thickness that is required for a meaningful second harmonic amplitude. Furthermore, the evaluation of a specimen with 2.6 cm thickness is a realistic application scenario. The length of the specimen is then chosen according to the angle of incidence and where the reflected P-wave is expected. In order to avoid interference with reflected waves additional 3 cm are added. The wedge and the specimen are modeled as one body. This idealization of the contact condition of the interface reduces computational effort. In the experiment the wedge gets attached to the specimen very firmly by the use of a couplant such as oil.

4.1.2 Material

The wedge is made of acrylic plastic and modeled to be linear elastic. The predefined material parameter of acrylic plastic in COSMOL were introduced in Chapter 3.1 in Table 3.1. The specimen is hyperelastic and made of aluminum with the material parameter of Table 3.2.

The hyperelasticity formulation of elastic energy density used in COMSOL is in accordance to Murnaghan description and accurate up to third order of approximation. This is equivalent to the the analytical consideration in this thesis. Higher terms are very small and have a negligible impact.

The nonlinear effects considered in this study are very small, but they are increasing with propagation distance, which can be achieved by larger angles or thicker specimens. In order to get significant amplitudes of the generated second harmonic wave field, which can be well separated from other effects of the discrete Fourier transform (DFT), our specimen has to be thick or long enough or the generated incident amplitude has to be significantly higher. But long propagation distances, that result in a larger specimen and longer simulation time, increase the computational expense heavily. Therefore, another possibility to increase the amplitude of the generated second harmonic is to increase the nonlinear effect, which does not impact the computational expense significantly. This is reasonable since the second harmonic wave amplitudes are linearly proprtional to the TOECs as shown in Figure 3.6.

Increasing the material nonlinearity and thereby increasing the nonlinear effect can be easily achieved by increasing the TOECs in the simulations. In order to compare the numerical results to the analytical results, these TOECs are increased by the same value in the analytical model. Therefore, the analytical approach can still be evaluated and verified and important qualitative results for an experimental setup can still be drawn. This approach has been already used by [27] simulating Rayleigh waves. Evaluation by means of the analytical approach and verification by the simulation results leads to a useful value for the increase factor of the TOECs of 100. This value is chosen for a model with the angle of around 50°, thickness of 0.026 m and a generated incident amplitude of 15×10^{-10} m. In the experiments the amplitude of the second harmonic is high enough due to significantly amplified A_i (compare Chapter 6). This is no possibility in the simulations since a generated incident amplitude comparable to the experiments would be computationally too expensive.

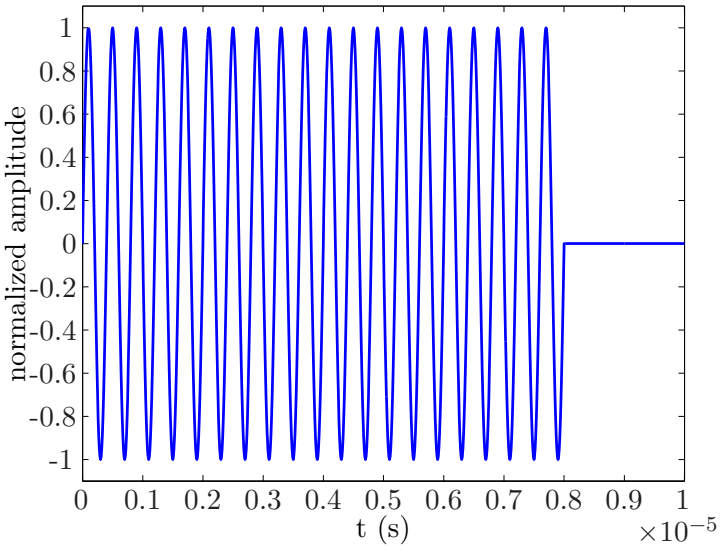

Figure 4.2: Normalized prescribed displacement for n = 20 cycles of sinus oscillations

4.1.3 Physics and boundary conditions

A prescribed displacement as a boundary condition (compare Figure 4.1) represents the transducer. This incorporates the idealization of the contact between wedge and transducer. In the experiment this ideal configuration is approximated by fixing the transducer with screws very firmly to the wedge. The excitation are $n = 12, 15, 20$ sinus oscillations with the frequency of 2.5 MHz and the peak amplitude of $A_i = 15 \times 10^{-10}$ as shown in Figure 4.2. Since a Gaussian distribution approximation of the amplitude generated by a transducer requires more than double the computational expense, the amplitude as a function of the position is approximated by a step function illustrated in Figure 4.3.

Since it is important that the specimen does not move, the specimen is fixed at both corners at the bottom. This mimics the typical experimental setup where the specimen is fixed at several points. The surface and bottom boundary are stress-free boundaries. The remaining boundaries are chosen to be low reflecting boundaries. The results of the simulations show that there are still reflection that cannot be neglected. So the reflections at every boundary has to be considered like in the experimental case.

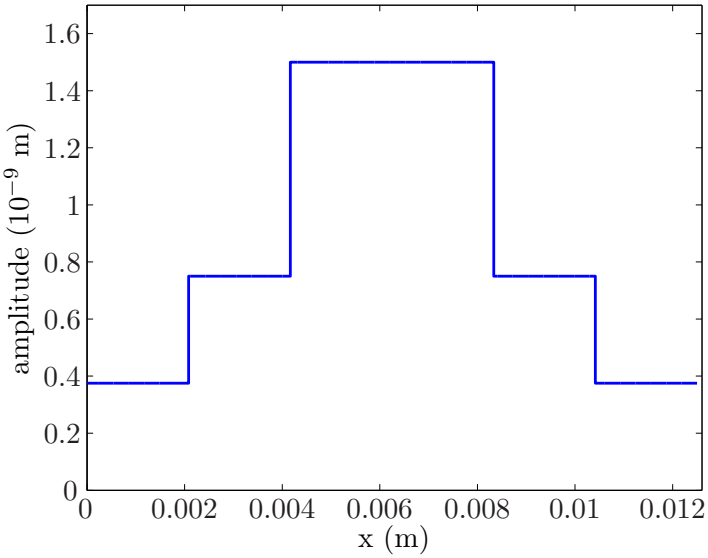

Figure 4.3: Amplitude of prescribed displacement of the transducer plotted over the boundary section that is representing the connection to the transducer

4.1.4 Mesh size, time steps and solver

The mesh size has to be chosen according to the smallest considered wave length. According to COMSOL [12] there should be around 5 - 8 mesh points per wavelength. Therefore, the mesh size for the presented model is chosen to be smaller than $c_{s2}/(5 \times 2 \times f_0) \approx 124.13$ μm. Accordingly, the maximum mesh size within the specimen is adjusted downward to 120 μm. Similarly the mesh size for the wedge is chosen. Since the wedge is linear elastic, only the first frequency has to be considered. Additionally, only a P-wave is generated by the transducer. Therefore, the mesh size is chosen to be smaller than $c_{p1}/(5 \times f_0)$, which results in a maximum mesh size of 160 μm. This implemented mesh size yields around 1.5 million degrees of freedom.

The time step should resolve the wave equally well in time as the mesh does in space. Larger time steps do not make optimal use of the mesh and can cause inaccurate results or endanger the convergence. Shorter time steps on the other hand lead to longer solution times with no considerable improvements to the results. The relationship between mesh size and time step is known as the Courant-Friedrichs-Lewy (CFL) ratio: $CFL = \frac{c\Delta t}{h}$, where Δt is the time step and h is the mesh size. In practice a CFL number of 0.2 proves to be

near optimal [12, 13]. Therefore, a time step of 4 ns is chosen in this research.

For the solver the Paradiso direct solver is applied. This solver is recommended by COMSOL [12]. Furthermore, it has its advantages in multi core calculations which are used in this thesis. Morlock [27] used this solver simulating second harmonic generation in Rayleigh waves. This indicates that this solver is also a good choice for second harmonic generation in bulk waves. Note that these parameters as well as solver have to be confirmed by variations as explained in Section 4.4.

4.2 Simulation

The model described in the former section is implemented in COMSOL. This section describes the computation and the signal processing that is used to obtain the results described in the following chapter.

4.2.1 Computation

The simulations in this thesis are conducted on the PACE clusters at the Georgia Institute of Technology. It is possible to run two or three simulations in parallel. The simulations are conducted on 4 cores and 16 gigabyte memory. The simulation time varies from 20 hours to 120 hours depending on the parameters, the size as well as how many results are saved during the computation.

4.2.2 Signal Processing

The signal processing is summarized and illustrated in Figure 4.4. The illustrated steps are explained in the following. First the x- and y-component of the displacement information of position 4 and 5 are imported to the signal processing program. In this thesis the signal processing was done with MATLAB. Since we want to accurately detect the second harmonic amplitude, we want the displacement information for each time step. Storage of that data for each meshing point of the specimen would result in huge files and long simulation times. Therefore, the exact displacement information is only stored for specific points, so called Domain Point Probes (DPPs), that are set at the stress-free surface. For evaluation or verification purposes the displacement information for the whole model can

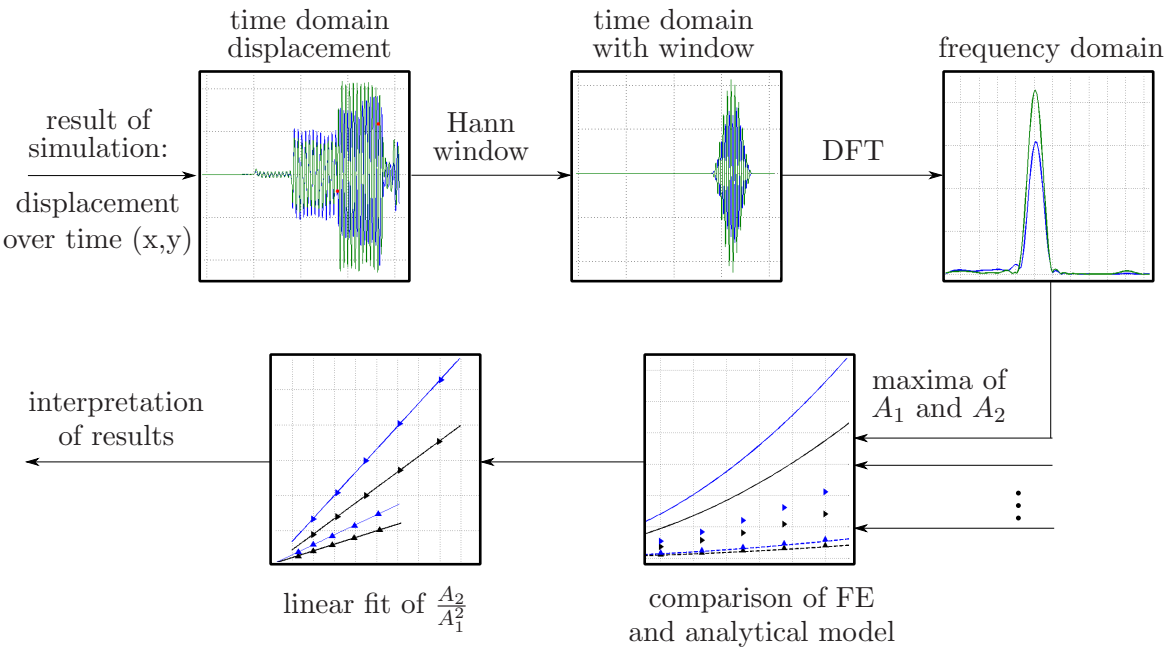

Figure 4.4: Signal processing of the simulation results

be saved for only specific points in time. The DPPs save the time domain displacement in material coordinates in x- as well as y-direction which is then imported into MATLAB. In order to extract the wave burst of interest, the arrival time and the signal length of the wave burst are calculated. The very beginning as well as the very end of the signal should not be used, such that on both sides a buffer of 1 - 2 cycles is applied in order to extract only the steady state wave. Since we want to transform the signal into the frequency domain, a Hann window is applied. The Hann window minimizes the amplitudes of the side lobes. Subsequently, we get the frequency domain plot shown in Figure 4.4 for the x- and y-component. In order to get the frequency domain amplitudes corresponding with the time domain amplitudes following formula has been used for the calculation

$$\text{time domain amplitude} = \frac{4 \times \text{frequency domain amplitude}}{\text{number of data points used for Hann window}} \tag{57}$$

Similar to [27], this approach has been chosen instead of summing up all the values near a maximum. This turned out to get more steady results since the range which has to be taken into account changes the result significantly.

After the DFT the maxima of the amplitudes of the fundamental wave and the second

harmonic wave can be calculated. This is done for the x- and y-component of the displacement at position 4 and 5 respectively. The simulation is then repeated for different parameters, for example increasing A_i. All the maxima are plotted with the corresponding analytical results and compared. Furthermore, the second harmonic amplitude is plotted over the squared fundamental amplitude. Like in many other experimental works, such as [22,26], those points are then linear fitted and the slope is calculated in order to compare the nonlinearity of different specimen.

4.3 First results and necessary improvements

In this section the results of the standard model are discussed and several problems are identified. The first conclusions about the simulation model as well as the experimental setup are drawn.

4.3.1 Results of the standard model

In order to evaluate the model and compare it to the analytical approach, the DPP are chosen at position 4, position 5 as well as position 1 and position 2. The time domain displacements in x- and y-directions are shown in Figure 4.5. It can be seen that the waves arrive at the calculated time marked by the red points. There are some unexpected waves that are further explained in Section 4.3.2 and 4.3.3. Furthermore, it can be seen that at position 2 and position 5 the signal has approximately the same amplitude in x- and y-direction, since the waves arrive at an angle of $\Theta_P = 50°$. At position 1, the amplitude in x-direction is significantly higher as the wave arrives at $\Theta_S = 22.64°$ and its nature is a S-wave. At position 4 there is a P-wave and a S-wave arriving. Therefore the difference in amplitudes in x- and y- direction should be in between position 1 and position 2. In Figure 4.6 the resulting displacements in the frequency domain are illustrated. Firstly, the fundamental wave at 2.5 MHz at all positions is presented. Secondly the second harmonic amplitude is illustrated. At bottom position 1 there is no second harmonic amplitude whereas at position 2, position 4 and position 5 there is another peak at 5 MHz. This is in accordance with the analytical results presented in the last two chapters. After the model is confirmed in this chapter, only the position 4 and 5 are of interest for the final results.

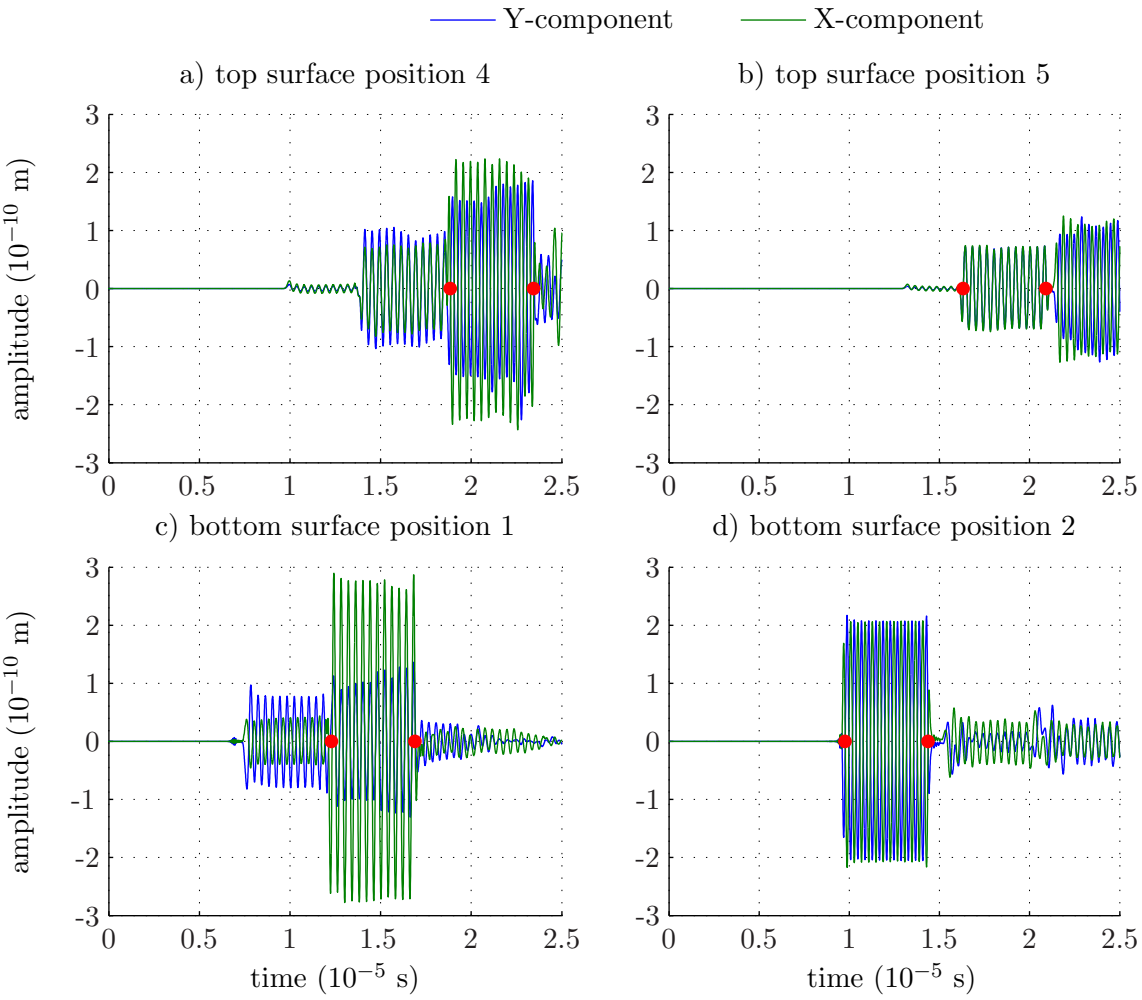

Figure 4.5: X- and y-component of the displacement field in the time domain at position 4, position 5, position 1 and position 2

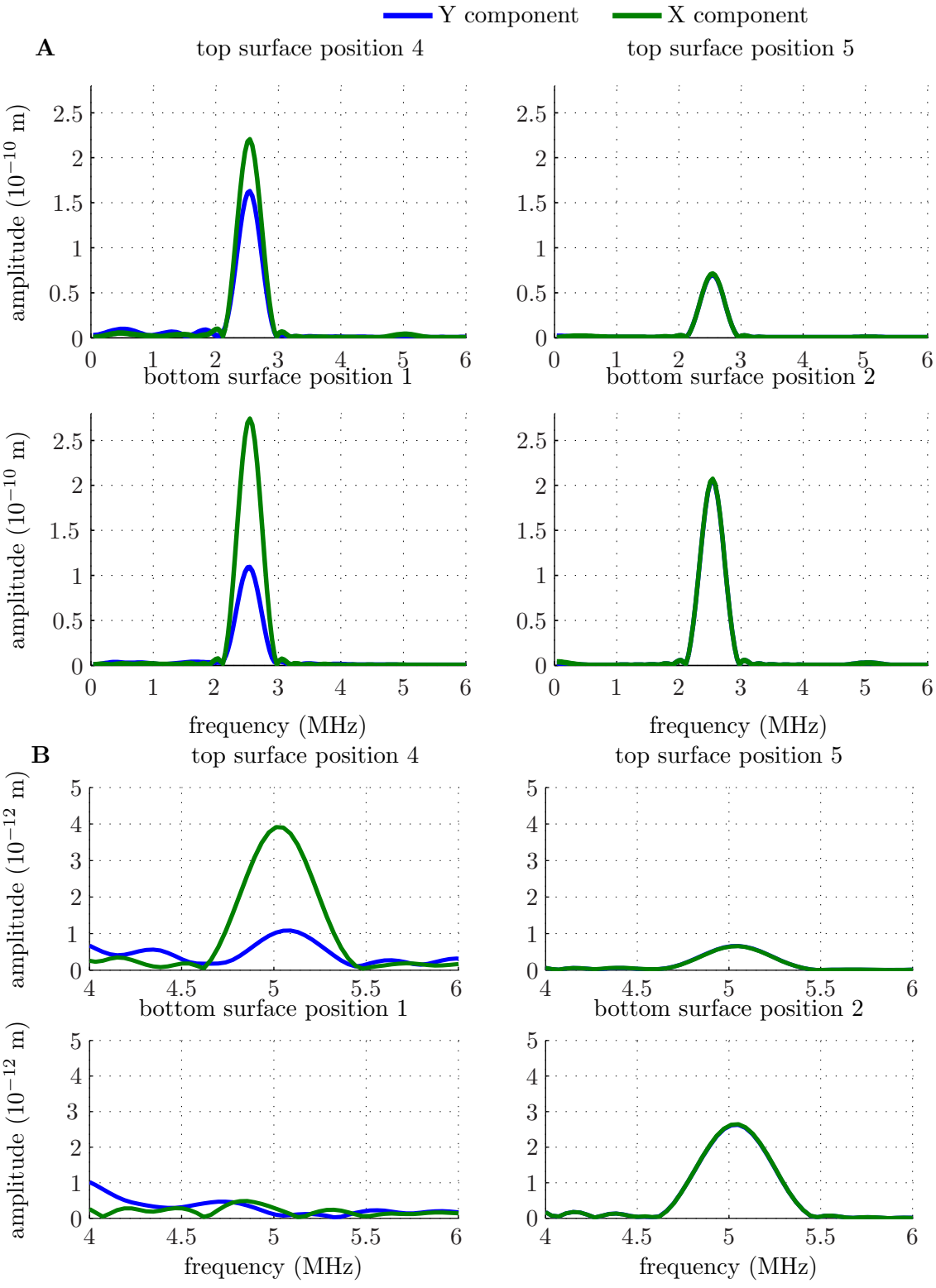

Figure 4.6: X- and y-component of the displacement field in the frequency domain at position 4, position 5, position 1 and position 2 plotted over all relevant frequencies in A and zoomed in for the second harmonic amplitude in B

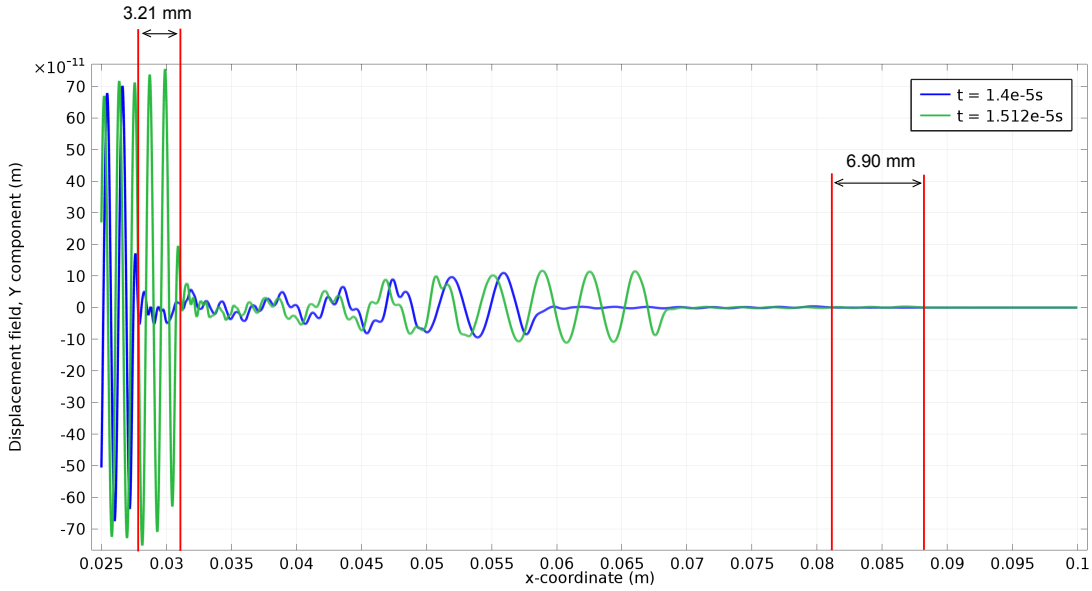

Figure 4.7: Y-component of the displacement field of the stress-free surface boundary at two different times revealing two surface waves

4.3.2 Avoidance of surface waves

In the first set of simulations there appear to be other arriving waves at position 4, which clearly influence the results. In order to investigate all the arriving waves, the displacement of the stress-free top surface boundary is evaluated at different times. In Figure 4.7 the displacement field of the stress-free top surface is plotted over the x-coordinate of the stress-free surface at two times $t = 1.4 \times 10^{-5}$ s and $t = 1.512 \times 10^{-5}$ s. Note that this stress-free top surface boundary starts at around $x = 25$ mm since that is where the wedge ends. There seem to be two surface waves, one with a very small amplitude traveling fast and one with a high amplitude traveling slowly. The wave velocities can now be easily evaluated with

$$c_1 = \frac{\Delta x}{\Delta t} = \frac{0.0069 \text{ m}}{(1.512 - 1.4)10^{-5} \text{ s}} = 6160.7 \frac{\text{m}}{\text{s}} \approx c_p = 6176.4 \frac{\text{m}}{\text{s}} \tag{58}$$

$$c_2 = \frac{\Delta x}{\Delta t} = \frac{0.00321 \text{ m}}{(1.512 - 1.4)10^{-5} \text{ s}} = 2866.1 \frac{\text{m}}{\text{s}} \approx c_r = 2889.0 \frac{\text{m}}{\text{s}} \tag{59}$$

where $c_r \approx \frac{0.862+1.14\nu}{1+\nu} c_s$. Accounting for the inaccuracy of determining the traveled distance these velocities correspond very well to the P-wave velocity and the Rayleigh wave velocity of the material. Consequently, there is a P-wave with a small amplitude traveling along the surface. This amplitude is negligible compared to arriving reflected waves. However, there

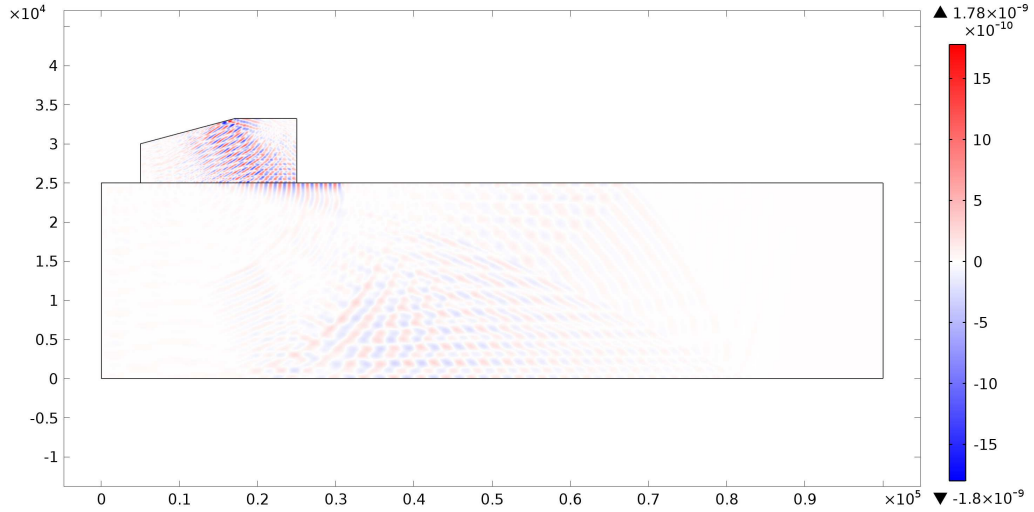

Figure 4.8: Y-component of displacement field of the specimen showing a Rayleigh surface wave originating at time $t = 1.5e - 5$ s

is also a Rayleigh wave traveling along the surface with the amplitude that is approximately twice as high as the amplitude of the reflected waves. Further investigating this Rayleigh surface wave in COMSOL we can see this wave originating and traveling in Figure 4.8 and 4.9 respectively.

A Rayleigh wave can only be formed by a very specific angle. Therefore, there must be a number of reflections within the wedge that finally cause a P-wave to arrive at the interface at this specific angle. In order to prevent this from happening, the geometry of the wedge has to be changed. Therefore a longer wedge is chosen and recommended for an experimental setup. With a longer wedge the reflected waves within the wedge cannot reach another angle than the starting angle within the simulation time. It is therefore recommended to carefully consider the geometry of the wedge when setting up an experiment. Comparing Figure 4.10 to Figure 4.8 it can be seen that the Rayleigh wave is eliminated with a longer wedge. The significant influence of a Rayleigh surface wave can be seen in Figure 4.11, where the received time signal with a short wedge and the received time signal with a long wedge are compared. The difference between those time signals is caused by the Rayleigh surface wave. The red dots represent the time of the arriving reflected wave burst of interest which is evaluated. Since the surface wave is arriving within the time slot of the arriving

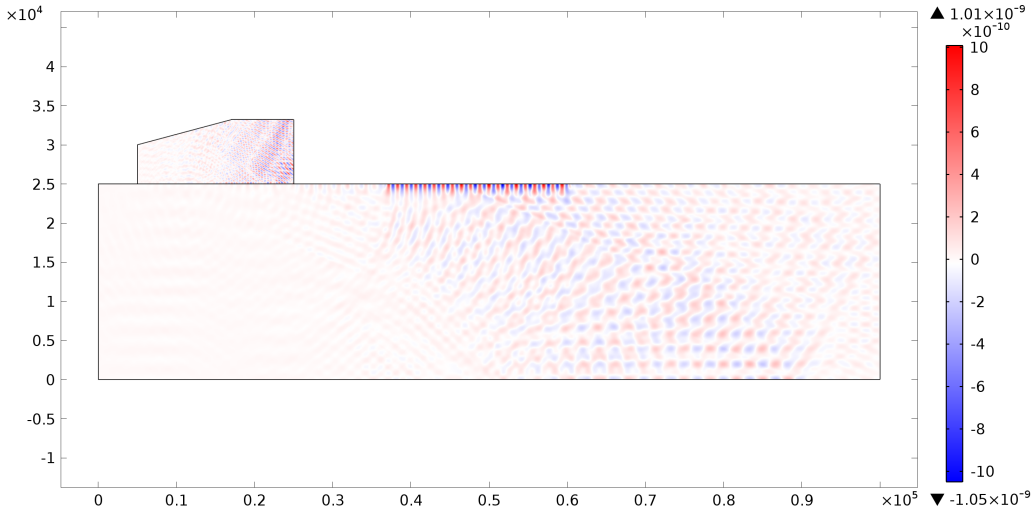

Figure 4.9: Y-component of displacement field of the specimen showing a Rayleigh surface wave propagating at time $t = 2.5e - 5$ s

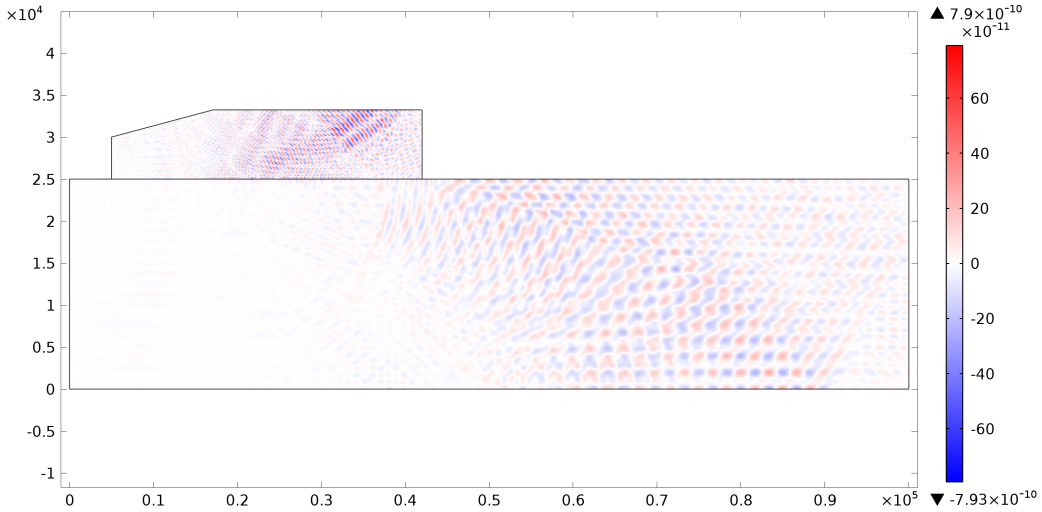

Figure 4.10: Y-component of displacement field of the specimen at time $t = 1.5e - 5$ s with a long wedge preventing the Rayleigh wave from originating

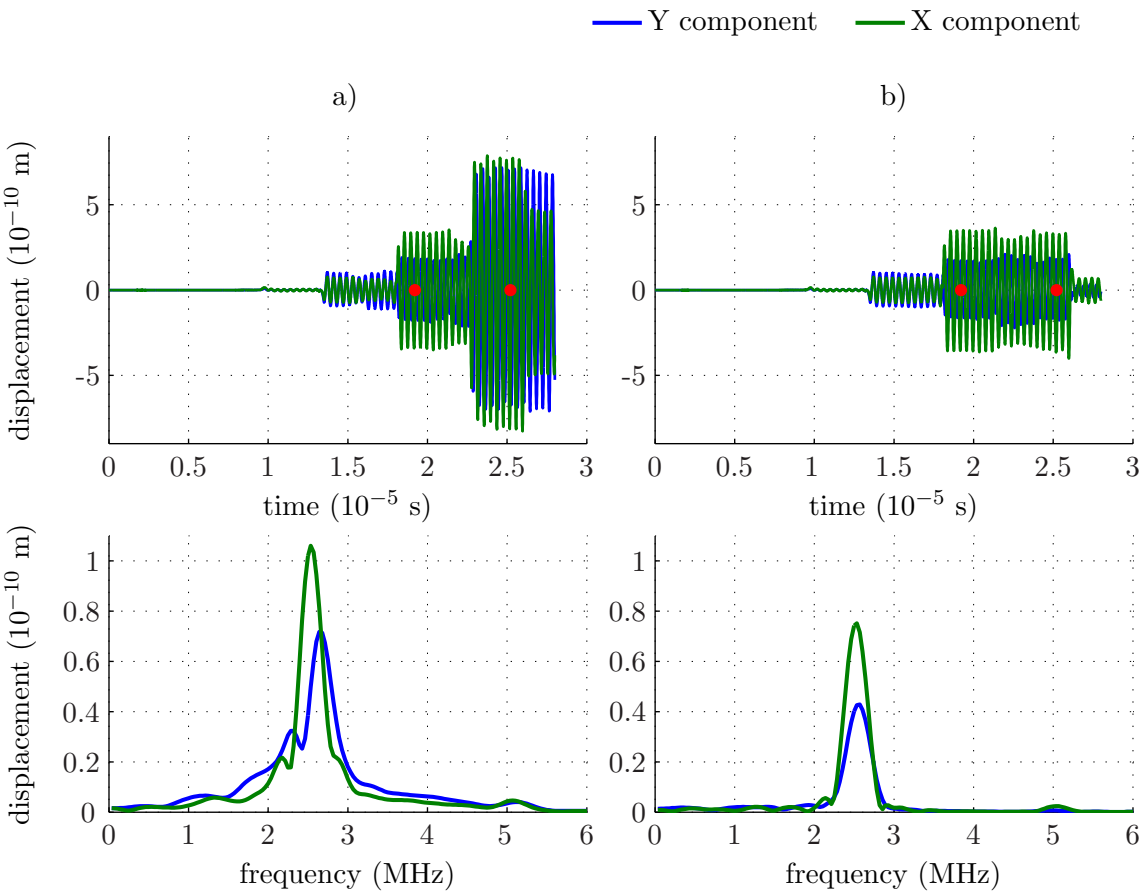

Figure 4.11: Displacement field at position 4 in the time domain and in the frequency domain for a) setup with short wedge, where a Rayleigh surface wave is generated and b) setup with long wedge

reflected wave, the frequency analysis cannot be used. Whereas with the long wedge the frequency analysis shows the anticipated result.

4.3.3 Avoidance of interaction with diffracted P-wave at position 4

In the analytical approach the plane wave assumption is used. However, in the simulations the diffraction of the bulk waves have to be considered. Therefore, there is also a faster propagating P-wave as part of the diffracted wave arriving at position 4. In order to preclude interaction which influences the results for position 4, the thickness of the specific specimen L and the number of cycles n have to be chosen according to following inequality

$$t_{p,disp} + t_{signal} < t_{wave} \tag{60}$$

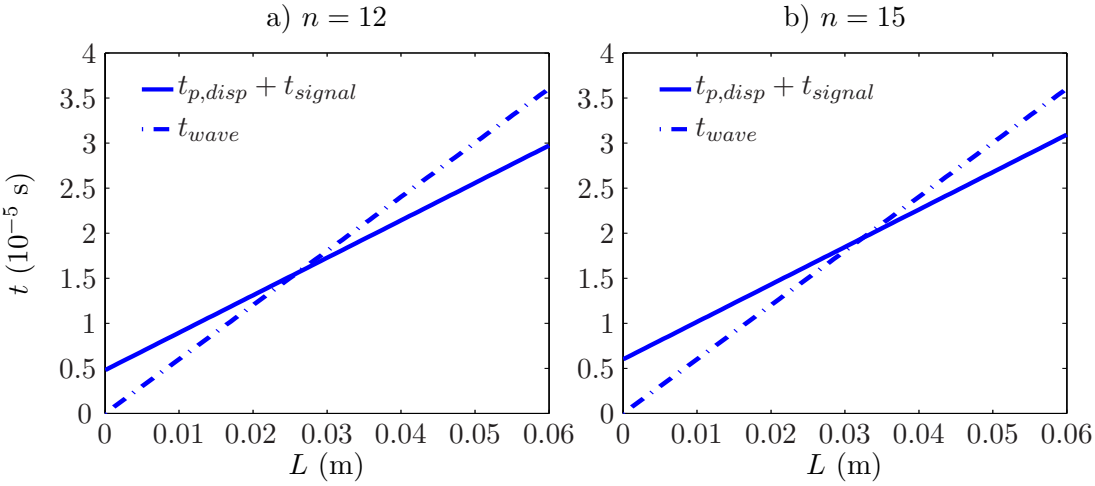

Figure 4.12: Illustration of L_{min} as the intersection of the signal length added to the arrival time of the diffracted P-wave and the arrival time of the actual signal for a) $n = 12$ cycles and b) $n = 15$ cycles

where $t_{p,disp}$ is the arrival time of the possible reflected P-wave, t_{signal} is the time length of the signal and t_{wave} is the arrival of the actual P- and S-wave of interest. This inequality expresses that the diffracted reflected P-wave has to be gone before the actual waves of interest arrive. This inequality can be represented in terms of numbers of cycles n, the frequency f, the thickness of the specimen L, the angle of the P- and S-wave Θ_P, Θ_S and the propagating velocities of the P- and S-wave c_P, c_S

$$\frac{\sqrt{(2L)^2 + (L\tan(\Theta_P) + L\tan(\Theta_S))^2}}{c_P} + \frac{n}{f} < \frac{L}{c_P\cos(\Theta_P)} + \frac{L}{c_S\cos(\Theta_S)} \tag{61}$$

In Figure 4.12 $t_{p,disp} + t_{signal}$ and t_{wave} are plotted over the thickness of the specimen L for two different number of cycles n. It can be easily seen that there is a thickness L_{min} at the intersection which should be smaller than the thickness of the specimen in order to avoid interaction. For a fixed setup the number of cycles should be chosen according to the thickness of the specimen. Figure 4.13 shows the maximum cycles n_{max} for a given thickness L. Therefore the number of cycles for the specimen of thickness $L = 0.026$ m is reduced to n = 12 cycles. In Figure 4.14 the time signal of $n = 15$ and $n = 12$ cycles is plotted. It can be easily seen that with $n = 15$ cycles the earlier arriving diffracted P-wave still has influence in the measured time frame marked by the two red points. With $n = 12$ cycles the diffracted P-wave has already passed and has no influence on the measurement

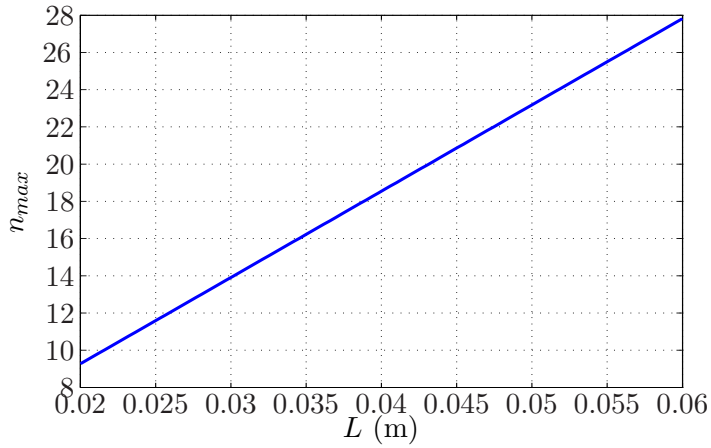

Figure 4.13: Maximum cycles n_{max} for a given thickness L in order to avoid interaction at position 4

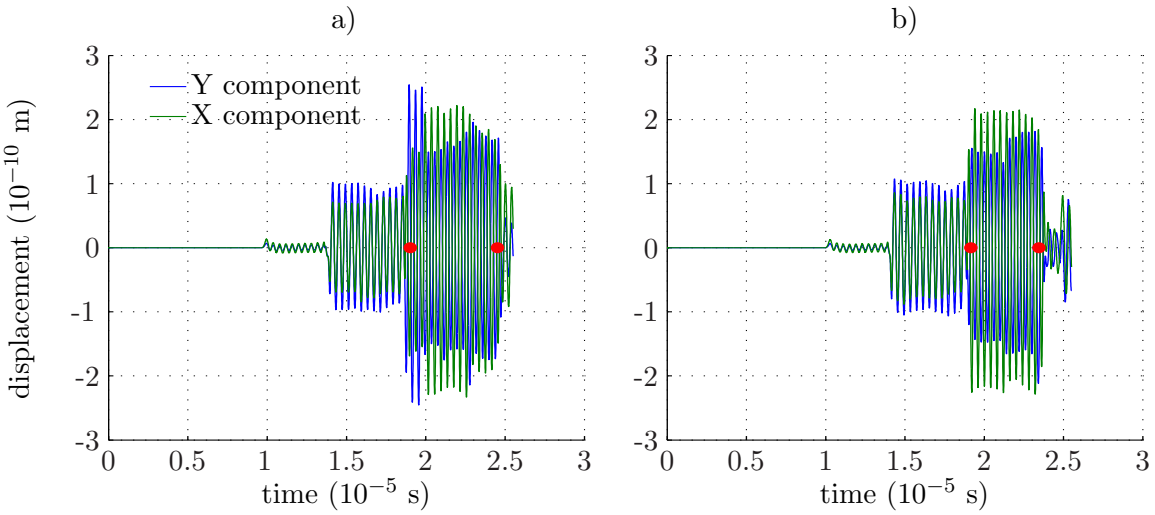

Figure 4.14: Displacement field at position 4 in the time domain for a) n=15 and b) n=12 cycles of generated sinus oscillations

anymore. This verifies Equation (61) derived in this chapter.

4.4 Confirmation of the finite element model

The FE model implemented in COMSOL has to be confirmed. Especially mesh size, time steps and the choice of the solver must not have an impact on the results. Therefore, mesh size as well as the time steps are chosen smaller for the confirmation of the implemented numerical model, and another solver is used. The difference between the results had a negligible impact on the qualitative results.

CHAPTER V

RESULTS OF THE SIMULATIONS

After the FE model was evaluated, improved and confirmed in Chapter 4 several simulations with varying parameters are conducted. The results are then compared to the analytical approach and the implementation in an experimental setup is evaluated. There are two important simulations with varying parameters that have to be investigated: increasing TOECs and increasing incident amplitude. The reason for this is that the recommended experimental setup in this thesis for the reflecting case is to measure the first and second harmonic amplitude over an increasing incident amplitude. Since the nonlinearity, and thus the TOECs, are linear to the second harmonic amplitude, the slope of A_2 over A_1^2 is proportional to the nonlinearity. Therefore, comparing the slope can potentially give absolute knowledge of the increase in the nonlinearity.

5.1 FEM results for suggested measurement model

In the first set of simulations the suggested measurement procedure is simulated. The generated incident amplitude A_i ranges from 1 nm to 2 nm and the material nonlinearity is increased by 50%. Note that if we consider the increase in all the simulations by the factor 100, this leads to an increase factor of 100 and 150.

In Figure 5.1 the absolute second harmonic amplitude is plotted over the generated incident amplitude for position 5 and position 4. It can be easily seen that the simulation results are considerably smaller than the analytical results but the tendency is in accordance with the analytical results. This is explained by the diffraction that is not taken into account in the analytical approach amongst others.

Note that for the comparison of the analytical and numerical results, the x-axis in numerous plots is chosen to be the incident amplitude A_i in this chapter. These figures have been constituted in that way because the incident amplitudes A_i for the numerical simulation were set according to values used in the analytical evaluation. Therefore, both

results can be plotted and compared regarding the values of incident amplitude A_i, whereas the resulting fundamental amplitude A_1 does not offer a common axis. Those figures serve for comparison purposes primarily; for the robustness and angle evaluating simulations and experiments only $\frac{A_2}{A_1^2}$ will be illustrated.

In Figure 5.2 the arriving second harmonic amplitude divided by the arriving fundamental amplitude $\frac{A_2}{A_1}$ is plotted over the incident amplitude A_i. By comparing the ratio, the simulation results in Figure 5.2 are closer to the analytical results than in Figure 5.1. This is because dividing by the arriving fundamental wave causes the diffraction effects to get relativized. Another important point to notice is that while at position 5 the relation between second harmonic and fundamental amplitude are almost the same in x- and y-direction, at position 4 there is a big difference. The reason for this is that at position 4 there are two waves arriving. The arriving second harmonic S-wave ${}_Su_{SrSr}$ has analytically the higher amplitude. This amplitude is only inclined by $\Theta_S = 22.64°$ out of the surface and therefore, the numerical results in the x-direction are similar to the analytical S-wave ${}_Su_{SrSr}$. The arriving P-wave ${}_Pu_{PrPr}$ on the other hand has a significantly smaller amplitude but it is inclined by $\Theta_P = 50°$ out of the surface. Therefore, the simulation results in y-direction are rather similar to the analytical P-wave ${}_Pu_{PrPr}$.

In Figure 5.3 A_2 is plotted over A_1^2. The points are then linearly fitted. It can be seen that the results are very linear and the R value for linear fitting is 0.9999. The R value for the linear fitting is a parameter to measure the correlation between the two vectors A_2 and A_1^2. It is the normalized covariance value: $R(A_2, A_1^2) = \frac{\mathrm{Cov}(A_2,A_1^2)}{\sqrt{\mathrm{Cov}(A_2,A_2)\mathrm{Cov}(A_1^2,A_1^2)}}$. It is now shown that position 5 as well as position 4 can be used for nonlinearity measurements. Especially for position 4 this result, the linearity of the second harmonic amplitude to the nonlinearity and the generated incident amplitude, is not trivial since there are two waves arriving.

5.2 Robustness regarding Hann window variations

For a good and repeatable measurement setup a certain robustness to variable parameters is important. Therefore, the used Hann window is changed in length and position in this

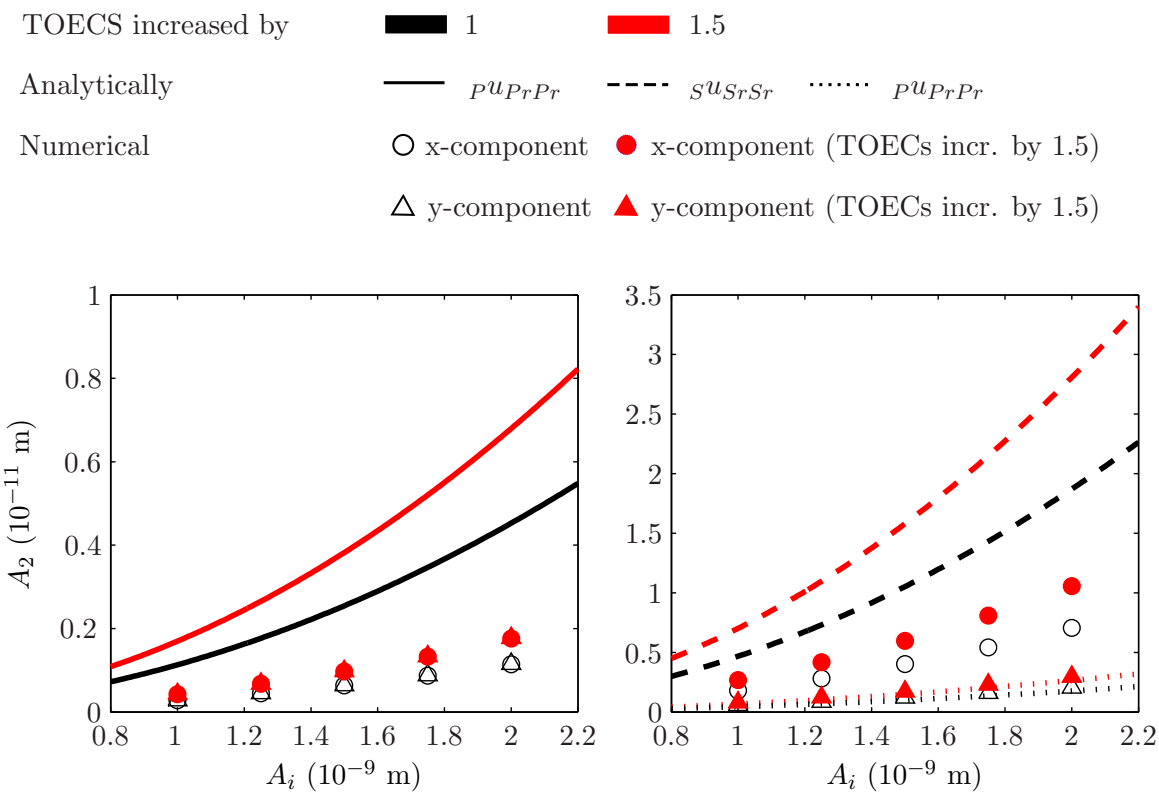

Figure 5.1: Second harmonic amplitude A_2 plotted over the generated incident amplitude A_i for a) position 5 and b) position 4

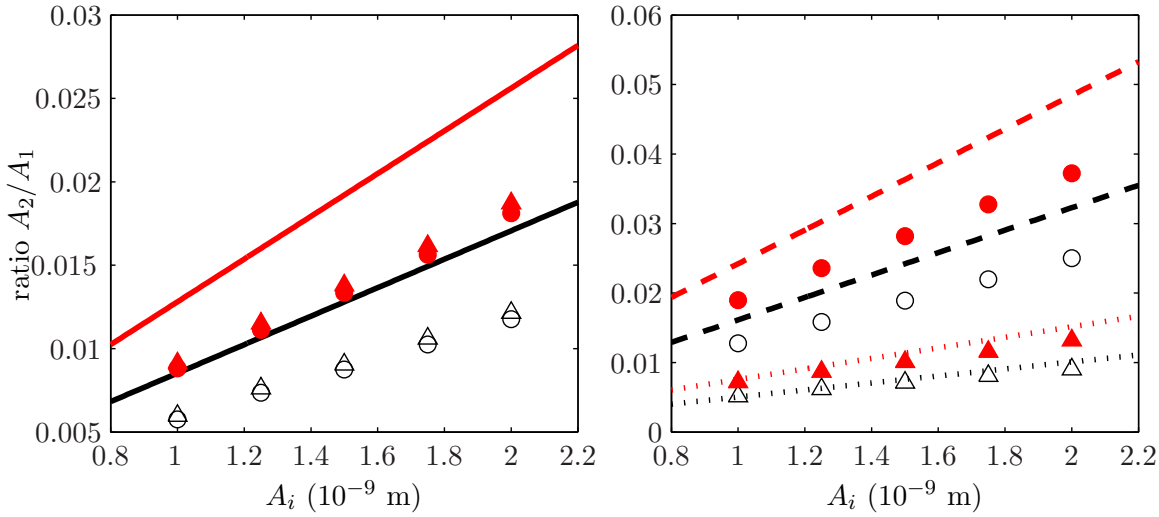

Figure 5.2: Arriving second harmonic amplitude A_2 divided by the arriving fundamental amplitude A_1 plotted over the incident amplitude A_i for a) position 5 and b) position 4

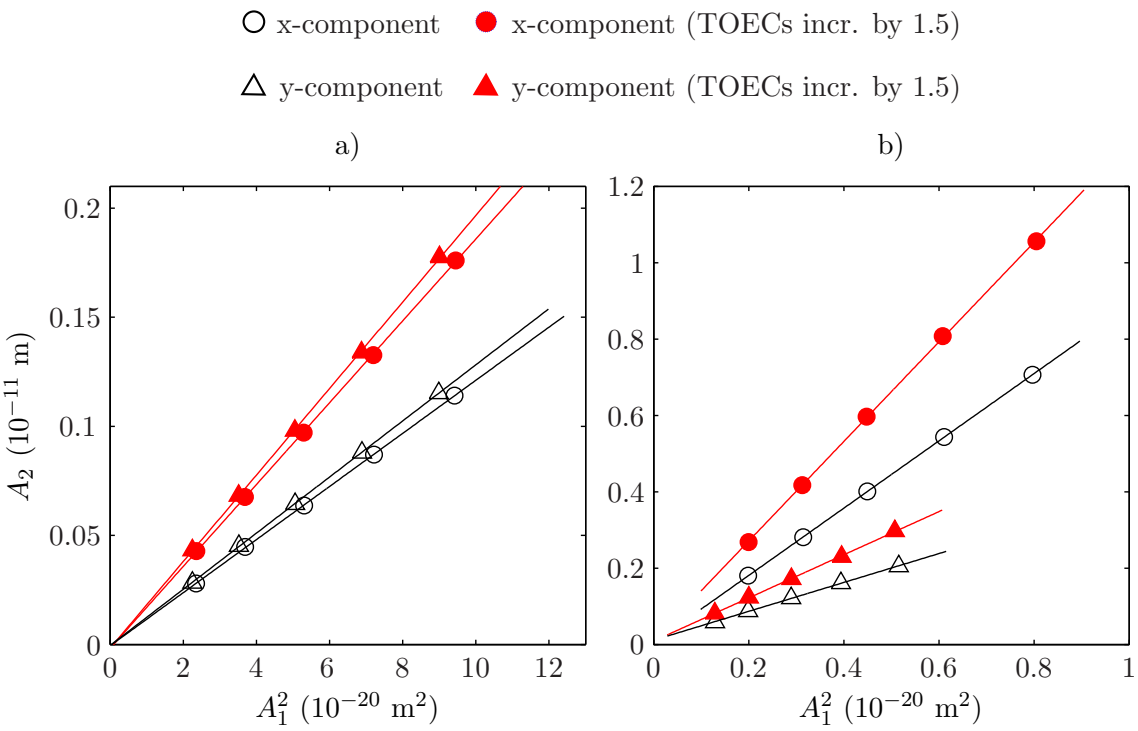

Figure 5.3: Linear fit of second harmonic amplitude A_2 plotted over squared fundamental amplitude A_1^2 for a) position 5 and b) position 4

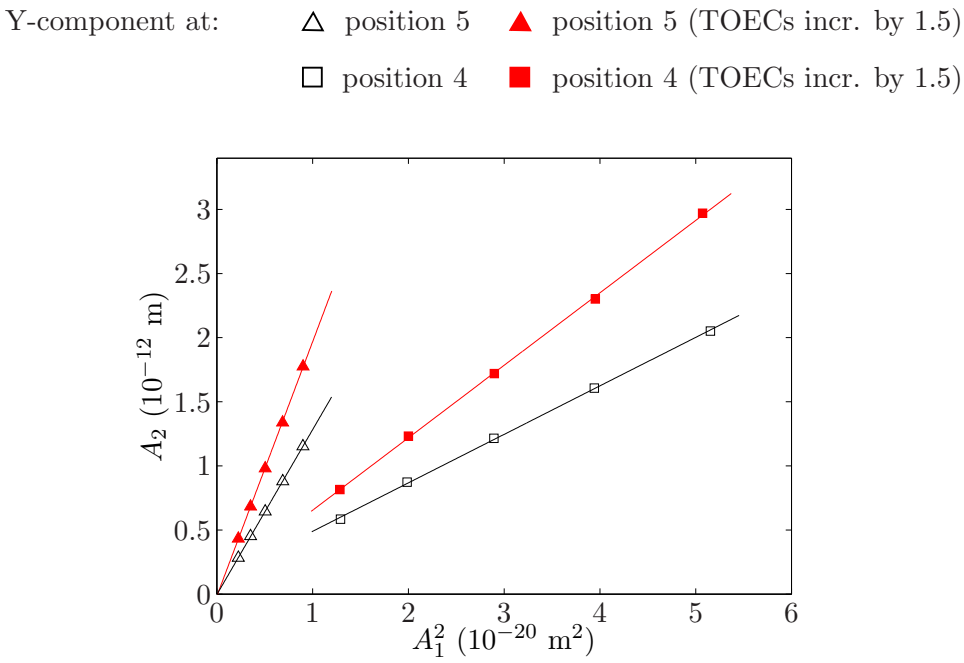

Figure 5.4: Comparison of linear fit of second harmonic amplitude A_2 plotted over squared fundamental amplitude A_1^2 in y-direction at position 4 and position 5

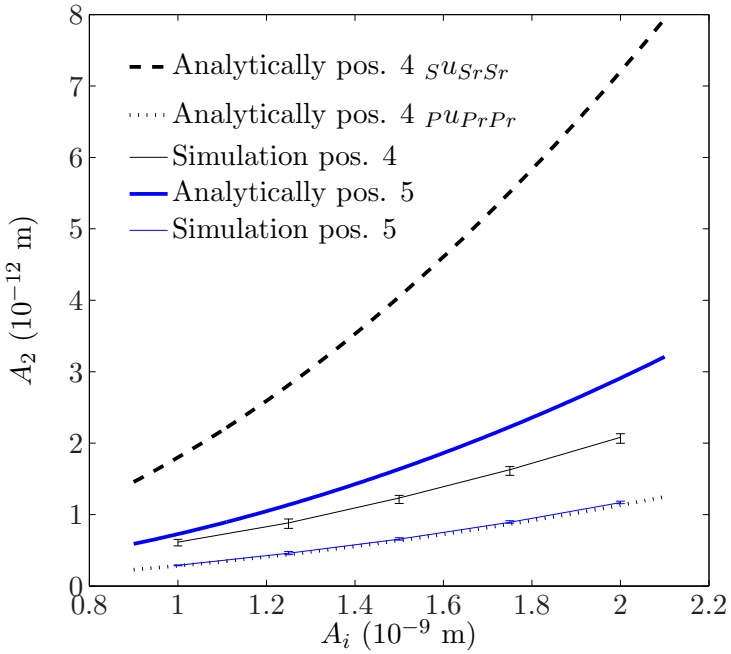

Figure 5.5: Second harmonic amplitude A_2 plotted over the generated incident amplitude A_i with varying Hann window regarding only y-components

section.

The results with errorbars are presented as absolute values of the second harmonic amplitude A_2 over an increasing incident amplitude A_i (Figure 5.5) and as arriving second harmonic amplitude A_2 over the squared arriving fundamental amplitude A_1^2 (Figure 5.6). In this simulation setup only the y-components are regarded since only the y-component can be measured in the experiments.

It can be seen that the amplitude of the second harmonic wave at position 5 varies significantly less than at position 4. But at both positions the correlation factors are close to 1 with R = 0.9987 and R = 0.9971 respectively, which confirms a good linear fit. Therefore, the variation of the Hann window does not have a significant impact on the results. However, position 5 shows more robustness.

5.3 Robustness regarding receiver position variations

For the next set of simulations the receiver was moved 1 and 2 mm to the right and to the left. The results with errorbars are also presented as absolute values of the second harmonic

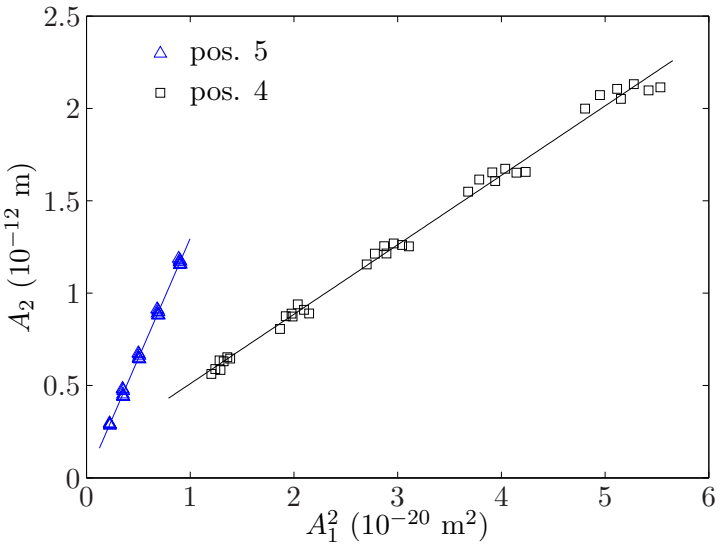

Figure 5.6: Linear fit of second harmonic amplitude A_2 plotted over squared fundamental amplitude A_1^2 with varying Hann window regarding only y-components

amplitude A_2 over an increasing incident amplitude A_i (Figure 5.7) and as arriving second harmonic amplitude A_2 over the squared arriving fundamental amplitude A_1^2 (Figure 5.8). The illustration is similar to the results with varying Hann window only regarding the y-component.

Again, the variation of the second harmonic amplitude is significantly higher at position 4, as illustrated in Figure 5.7. Figure 5.8 shows that the variations with shifted receiver are higher compared to the results with varying Hann window. The correlation factor is still close to 1 with R = 0.99288 and R = 0.99282 what shows the robustness of the measurement method. Similar to the results of the variation of the Hann window, position 5 turns out to be more robust.

5.4 Recommendation for experimental setup

5.4.1 Receiver position

In order to decide whether position 4 or position 5 should be recommended for the receiver position, one has to take into account the absolute amplitude of the second harmonic arriving at that position as well as how accurate and repeatable the measurements can be at that position.

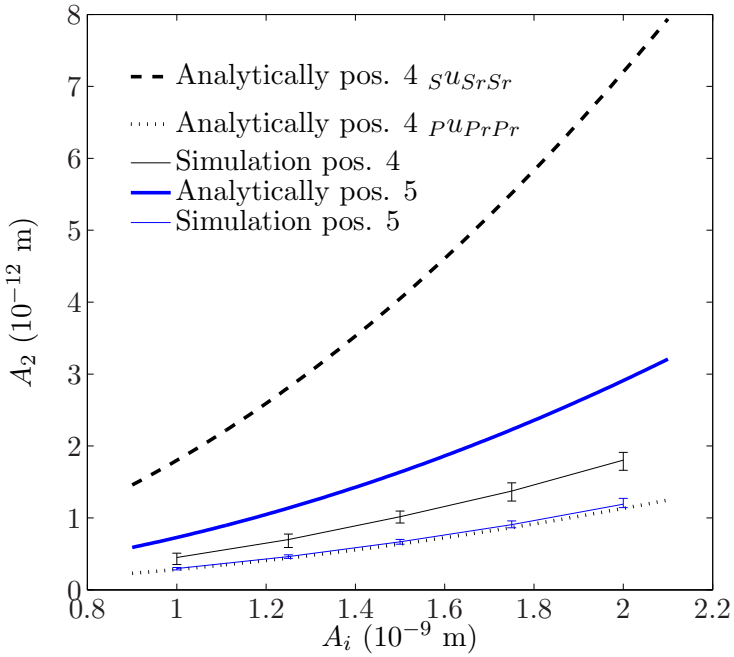

Figure 5.7: Second harmonic amplitude A_2 plotted over the generated incident amplitude A_i with shifted receiver (± 1-2 mm) regarding only y-components

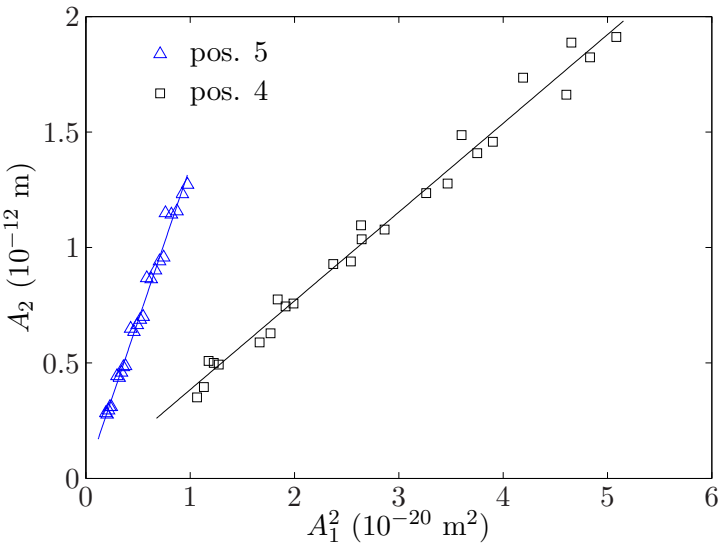

Figure 5.8: Linear fit of second harmonic amplitude A_2 plotted over squared fundamental amplitude A_1^2 with shifted receiver (± 1-2 mm) regarding only y-components

For reliable measurements, the second harmonic amplitude should be as large as possible with respect to the noise level. Therefore, position 4 has an advantage considering the absolute amplitude. As seen in Figures 5.5 and 5.7, for example, the second harmonic amplitude for $\Theta_P = 50°$ is 30%−50% larger at position 4 than at position 5. For larger angles this percentage is supposed to increase. For smaller angles on the other hand the difference will get more insignificant. For angles smaller than 40° the amplitudes are supposed to be in the same range (compare Figure 3.8).

Considering the robustness of measuring, Figure 5.5 and 5.7 suggest that the variation at position 5 is smaller regarding varying windows or shifting the receiver. Furthermore, position 4 is more vulnerable for interference of any type since the propagation velocity of the S-wave is smaller than the propagation velocity of the P-wave. Another point is that position 5 is more robust concerning the calculation of the arrival time because one can take the first waves arriving. Furthermore, even though the results of the simulations showed that the interaction of two arriving waves at position 4 does not impact the linearity that is necessary for the measurement procedure, inconsistencies of each wave can add up.

All in all the resulting suggestion in this thesis is to measure at position 5. Firstly the amplitude difference is negligible for angles less than 40° and acceptable to angles less than 60°. In return the robustness of measuring at position 5 is definitely higher.

5.4.2 Incident angle

Another parameter that has to be determined for the measurement setup is the incident generated angle that is optimal for the receiver at position 5. Analytically, the second harmonic amplitude is supposed to increase with the angle, since the propagation distance gets longer but on the other hand the angle changes in favor of the x-component. This analytically results in a slightly increasing y-component of the second harmonic amplitude with an increasing angle (compare Figure 3.8). In the simulation, diffraction is included. The diffraction effect increases with larger angles and therefore longer propagation distances. Therefore, the second harmonic amplitude now finds an optimum at around $\Theta_P = 35°$ as

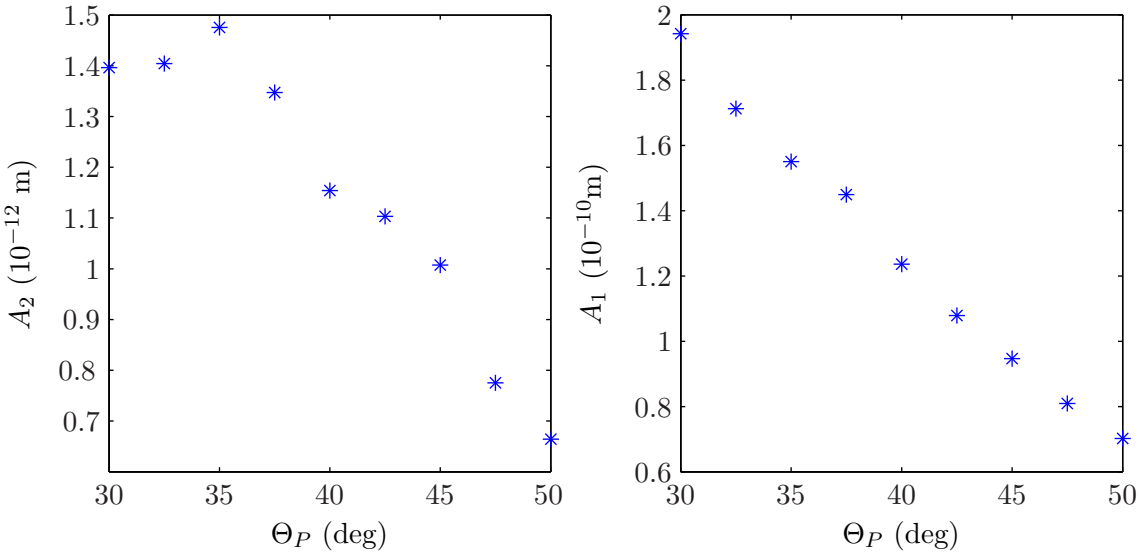

Figure 5.9: Y-component of the second harmonic amplitude A_2 and fundamental amplitude A_1 plotted over increasing angles Θ_P of the P-wave

seen in Figure 5.9. Note that the diffraction effect will be much higher in an experimental setup since a 2D model was chosen in the simulations. Also note that attenuation is not included, but the analytical evaluation showed a negligible impact of attenuation in aluminum compared to other impacts.

The fundamental amplitude is decreasing drastically with larger angles as shown in Figure 5.9. This has several reasons. Firstly, the reflection coefficient of the P-wave decreases with larger angles as shown in Figure 3.3 and secondly because there is more diffraction due to larger angle and longer propagation distances. Furthermore, the out-of-plane part of the displacement decreases with increasing angle.

Plotting A_2/A_1^2 over the propagation distance in Figure 5.10, it can be clearly seen that this ratio increases with propagation distance and therefore with larger angles. But because of diffraction this increase is damped compared to the analytical solution. Also in the analytical solution, the linearity of $\frac{A_2}{A_1^2}$ over propagation distance is slightly attenuated by the decreasing reflection coefficient of the P-wave at the stress-free boundary for increasing angles.

Since the absolute amplitude of the second harmonic has an optimum at around $\Theta_P =$

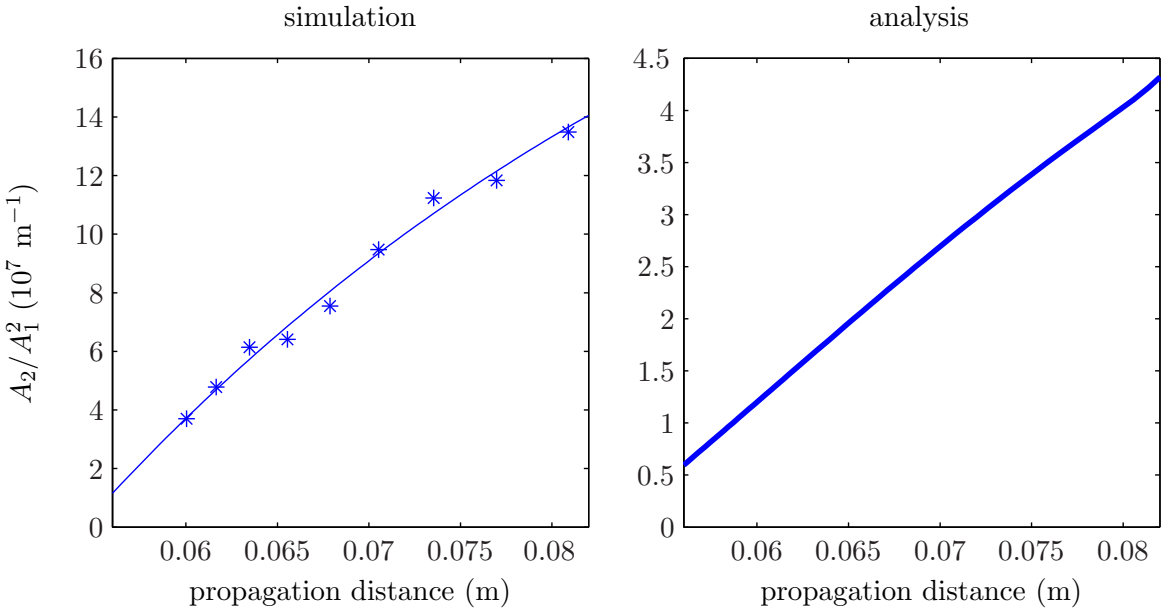

Figure 5.10: A_2/A_1^2 plotted over increasing propagating distance due to increasing angles

35°, but the slope of $\frac{A_2}{A_1^2}$ increases with propagation distance, angles between $\Theta_P = 35° - 45°$ are recommended and chosen for the experimental setup. This recommendation is also in accordance with the NDE application of measuring local defects.

The results of the simulations verify the analytical approach taking into account assumptions and approximations of the analytical solution procedure. Furthermore, the simulations show more robustness at position 5, which is the recommended measurement position. When choosing position 4 the number of generated sinus cycles should be chosen according to the derived Equation (61). For the recommended measurement position 5, an optimal angle of approximately $\Theta_P = 35° - 45°$ is determined. All in all, the feasibility of the suggested measurement method is numerically confirmed. In the next Chapter the suggested measurement method is applied in an experiment, evaluating the application and feasibility in an experimental setup.

CHAPTER VI

EXPERIMENTS

The measurement technique, that has been evaluated analytically and in simulations, is applied experimentally in this chapter. First, the experimental setup is introduced. Then the experiment conduction and its results are presented. Since only relative information about the nonlinearity are accessible by this measurement procedure, two different aluminum specimen are used in order to compare their nonlinearity. Furthermore, the robustness of position 4 and position 5 are evaluated on the basis of the experimental results.

6.1 Experimental Setup

The experiment was conducted as seen in Figure 6.1. A function generator, a 80 MHz 33250A arbitrary waveform generator from Agilent, generates sine waves at $f_0 = 2.5$ MHz. Since position 4 and position 5 are evaluated in the experiments, the number of cycles of generated sinus oscillations is determined by Equation 4.3.3. As the specimens are 0.0254 m thick, 12 cycles of sinus oscillations are used. This signal then gets amplified by a high power gated amplifier RITEC GA-2500A. This is very important because the amplitude of the fundamental wave has to be large enough for the second harmonic wave to be generated. The amplified signal is send to a transmitting transducer. A piezoeletric transducer of KB-aerotech type gamma centered at 2.25 MHz has been selected. It converts the electrical signal into longitudinal displacements. The transducer is screwed onto a variable-angle wedge as shown in Figure 6.1. This enables to send the longitudinal wave into the wedge at an oblique angle. The transducer is coupled to the wedge with oil. Similarly, the whole wedge is attached to the specimen with screws and oil coupling. As material properties, the longitudinal wave speed is given as $c_{p,wedge} = 2720\frac{m}{s}$. The experimental setup is shown in Figure 6.2.

First, the longitudinal wave travels through the wedge. At the solid-solid interface, the

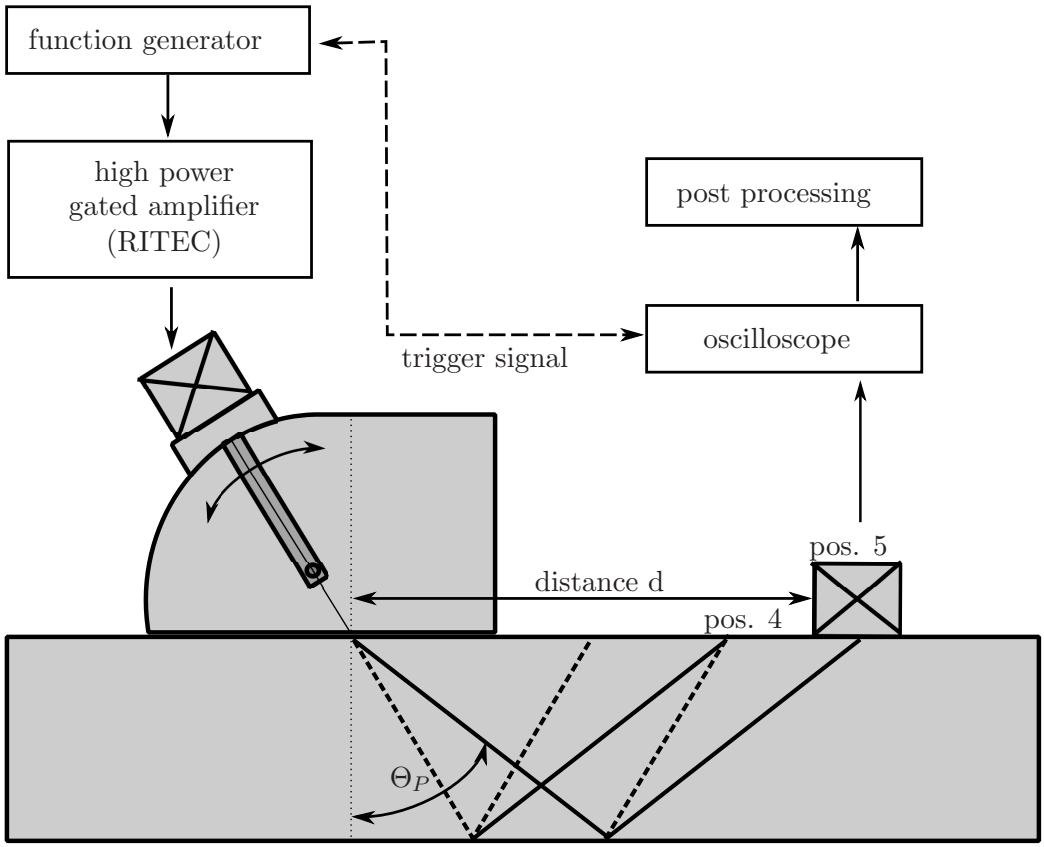

Figure 6.1: Experimental approach

wave is reflected and transmitted according to Section 2.1.3. The transmitted S- and P-wave are then traveling through the specimen and get reflected at the stress-free boundary. During the propagation in the specimen and at the stress-free boundary higher harmonics are generated. Usually only the fundamental and the second harmonic amplitude can be measured. For the detection of these wave components a receiver is positioned at position 4 or position 5 respectively. The receiver has been selected to be a piezoeletric P-wave transducer of Panametrics centered at 5 MHz with emphasis on the second harmonic frequency. This transducer is attached to the specimen with screws and oil coupling to detect the out of plane displacement. The signal is then send to the oscilloscope, a DPO 5034B Digital Phospor Oscilloscope of Tektronix, where the digitized signal is displayed and processed. In order to reduce noise, an average of 265 signals is taken and saved. Similar to the simulations, the post processing was done in MATLAB. The experimental post processing is illustrated in Figure 6.3.

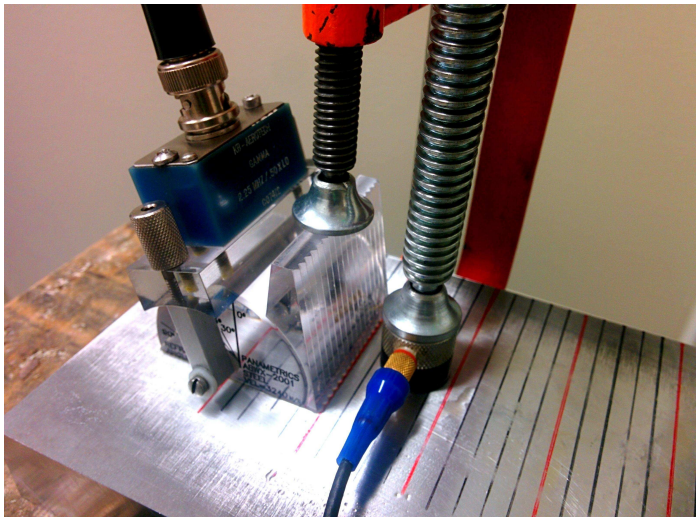

Figure 6.2: Experimental setup

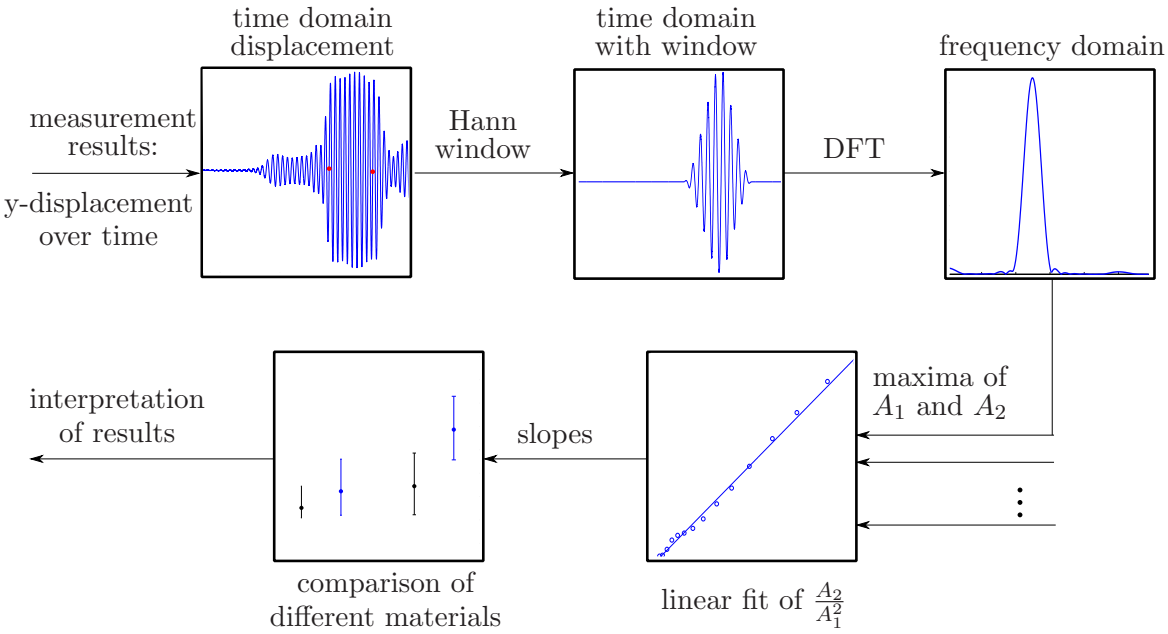

Figure 6.3: Signal processing of the experimental data

6.1.1 Specimens

First, an aluminum 2024-T351 specimen with 25.4 mm thickness is used in the experimental setup. The Al 2024-T351 plate is heat treated at 325° for three hours followed by air-cooling. Since only the relative nonlinearity parameter β^{rel} can be determined, another specimen is measured as a reference. The second specimen is chosen to be an aluminum 7075 specimen with the same thickness. Using two aluminum specimen improves the comparability between the two β^{rel} values since the linear ultrasonic properties are assumed to be equal. For both materials there are nonlinearity values available in the literature [24, 33]. Both specimen are hand-polished using 800 grad sandpaper in order to get the same surface and coupling conditions.

6.2 Experimental Results

Initially, basic tests are performed to see whether position 4 and position 5 can be determined and the corresponding waves can be identified. For these initial tests the receiving transducer is attached in a distance of 4 cm of the transmitting transducer. The incident angle is set up according to the calculated angle shown in Table 6.1. But the angle is difficult to adjust accurately and a change of 2° results in a position variation of the detecting device of approximately 8 mm (compare Table 6.1). Therefore, it is very important to adjust receiver position and angle to find the peak amplitudes of the waves we are interested in. Here, first the angle is changed slightly to get the peak amplitude followed by fine tuning by moving the receiving device.

The sound rays near the boundary of the incident wave have slightly different incident angles, which causes slightly different nonlinear interaction with the free boundary. This results in a distorted second harmonic wave field, whose amplitude is location-dependent. Therefore, the measurement should ideally be taken from the center of the beam. Consequently, finding the peak of the amplitude is important for accurate results.

As shown in Figure 6.4 and Figure 6.5, both detecting positions and the according waves can be identified. The time domain signals look similar to the time domain signals from the simulations shown in Figure 4.5.

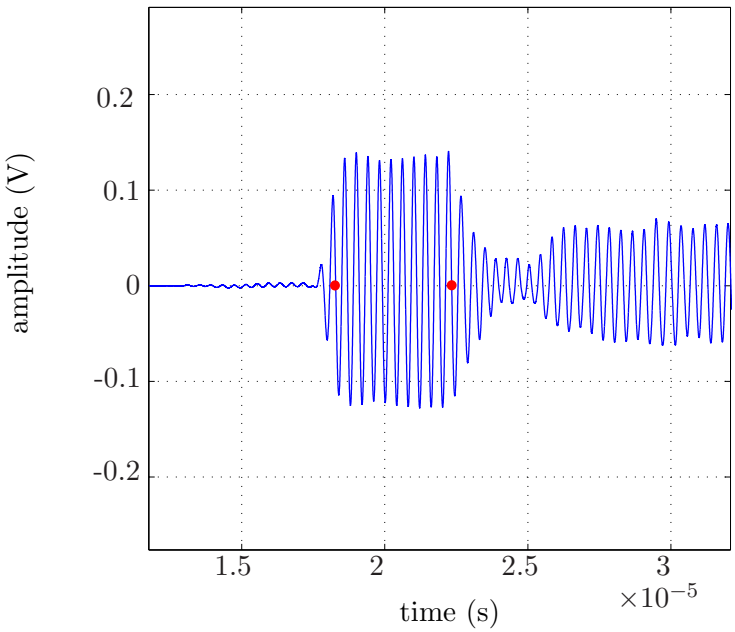

Figure 6.4: Measured time domain signal at position 5

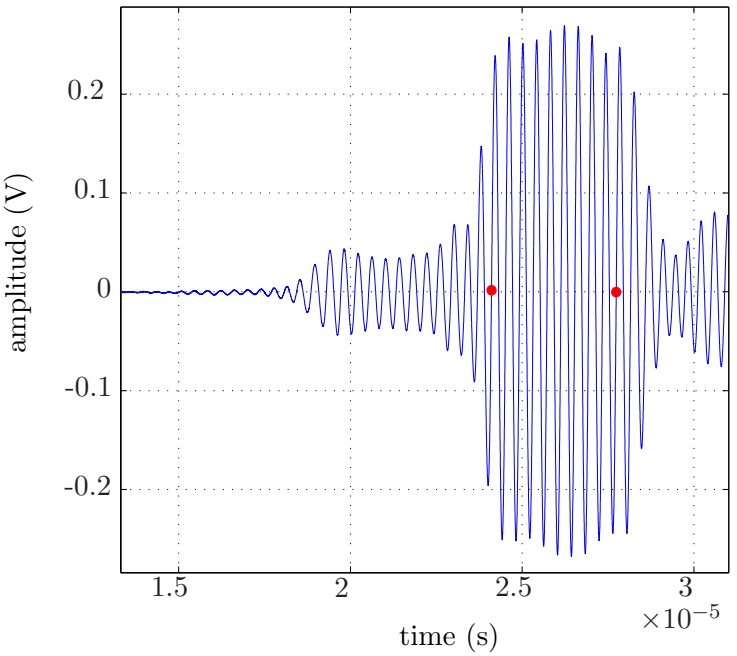

Figure 6.5: Measured time domain signal at position 4

Table 6.1: Possible measurement setup values

Θ_P	Θ_i	position 4	position 5
35.0°	14.6°	2.5 cm	3.5 cm
38.7°	16.0°	2.8 cm	4.0 cm
42.0°	17.1°	3.1 cm	4.5 cm
45.0°	18.1°	3.5 cm	5.0 cm
47.7°	19.0°	3.7 cm	5.5 cm
50.0°	19.7°	4.0 cm	6.0 cm

When the setup with the peak amplitude of the waves of interest is found, the nonlinearity measurement can be conducted. The input voltage is gradually increased and the time domain signal is saved and processed. For each input voltage amplitude, the arriving fundamental and second harmonic amplitude is determined. Plotting the second harmonic amplitude A_2 over the squared fundamental amplitude A_1^2 shows a good linear fit, as shown in Figure 6.6. Ideally the slope is now proportional to β, the nonlinearity of the material. But in reality, part of the measured nonlinearity is due to the inherent system nonlinearity from the instrumentation and coupling. In order to account for the inherent system nonlinearity the measurement setup can be calibrated as described in Section 6.2.1. But using the same measurement setup to determine changes in the nonlinearity of a material, the calibration is not necessary.

This slope is determined numerous times for each specimen, where transducer and receiver are reattached at the same position each time. Initially, this slope is determined for position 4 and position 5 of the Al 2024 specimen in order to compare the robustness of the two measurement positions. The results are shown in Figure 6.7.

Comparing the errorbars at position 5 to position 4, the variance at position 4 is significantly higher than at position 5. While the spatial variation at position 5 is within $\pm$ 20%, the variation at position 4 is approximately $\pm$ 40%. This validates the result of the simulations that position 5 is more robust than position 4. Note that this is only a comparison of position 4 and position 5 regarding the variation and not regarding the slopes and the β^{rel} values respectively. The slopes at position 4 and position 5 are supposed to be different, as shown in the previous chapters.

Secondly, the β^{rel} for both aluminum samples at position 5 is determined and compared

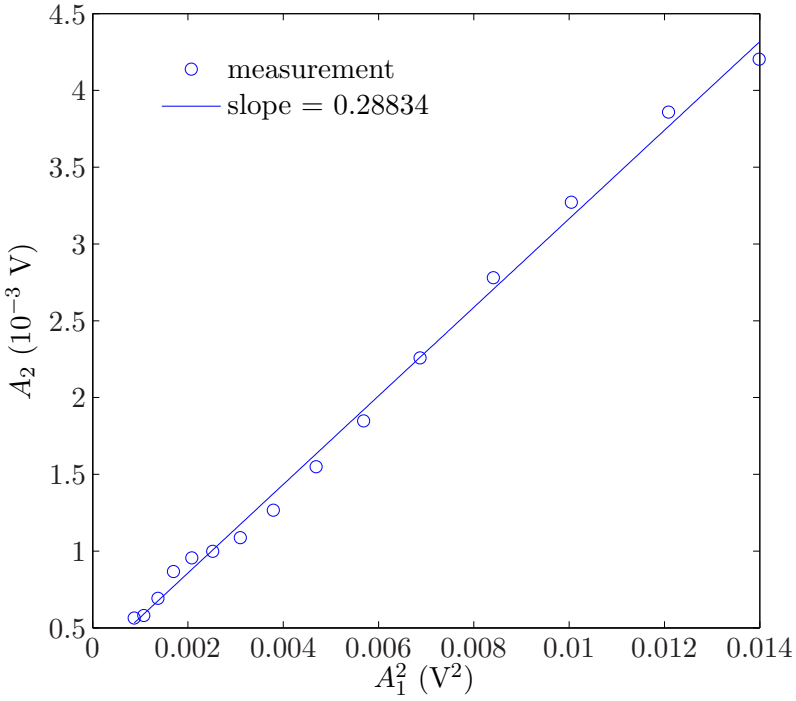

Figure 6.6: Linear fit of measured amplitudes A_2 to A_1^2 in order to determine the slope

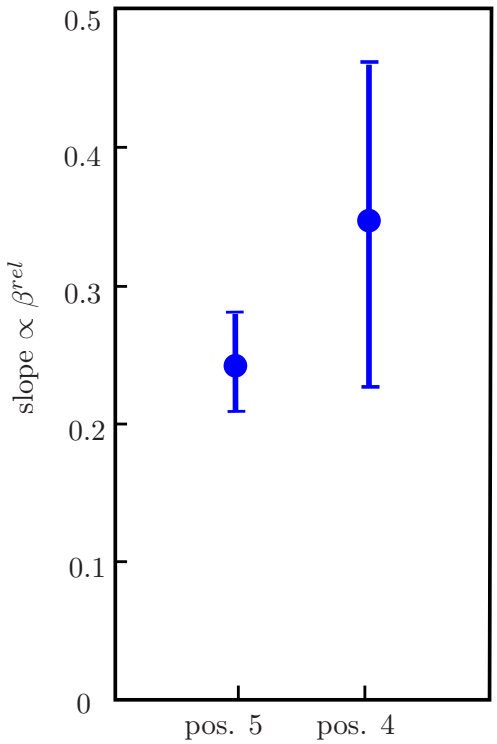

Figure 6.7: Comparison of the robustness of the relative β^{rel} values at position 5 and position 4 for Al 2024

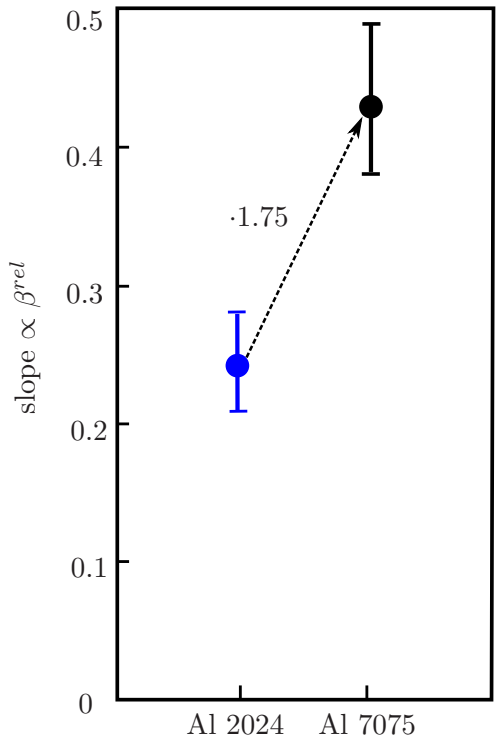

Figure 6.8: Comparison of the relative nonlinearity parameter of Al 2024 and Al 7075 obtained by using the reflection at a stress-free boundary

Table 6.2: Relative nonlinearity parameter obtained by using the reflection at a stress-free boundary

β^{rel}_{Al7075}	0.42 ± 20 %
β^{rel}_{Al2024}	0.24 ± 20 %
$\beta^{rel}_{Al7075}/\beta^{rel}_{Al2024}$	≈ 1.75

at a distance $d = 4.0$ cm, which corresponds to $\Theta_P = 38.7°$. The results are illustrated in Figure 6.8, which shows a clear increase of nonlinearity from the Al 2024 specimen to the Al 7075 specimen. The according β^{rel} values are presented in Table 6.2.

In order to validate these results by comparison with literature values, the ratio of the relative values $\beta^{rel}_{Al7075}/\beta^{rel}_{Al2024}$ is calculated and also added to Table 6.2. Nonlinearity values for the two aluminum specimen are presented in [24,30,33]. Thiele et al. [30] uses an air-coupled receiver for the measurement of the nonlinearity with Rayleigh surface waves. Li et al. [24] and Yost and Cantrell [33] use a capacitive receiver measuring the second harmonic generation in longitudinal waves. As noted by Thiele et al. [30], a one-to-one comparison is difficult to make because slightly different chemical compositions and heat

Table 6.3: Resulting nonlinearity ratio in comparison with literature values

reference	this research	[30]	[33]	[24]
$\beta_{Al7075}/\beta_{Al2024}$	≈ 1.75	1.50 - 1.85	1.70 - 2.03	0.97 - 1.28

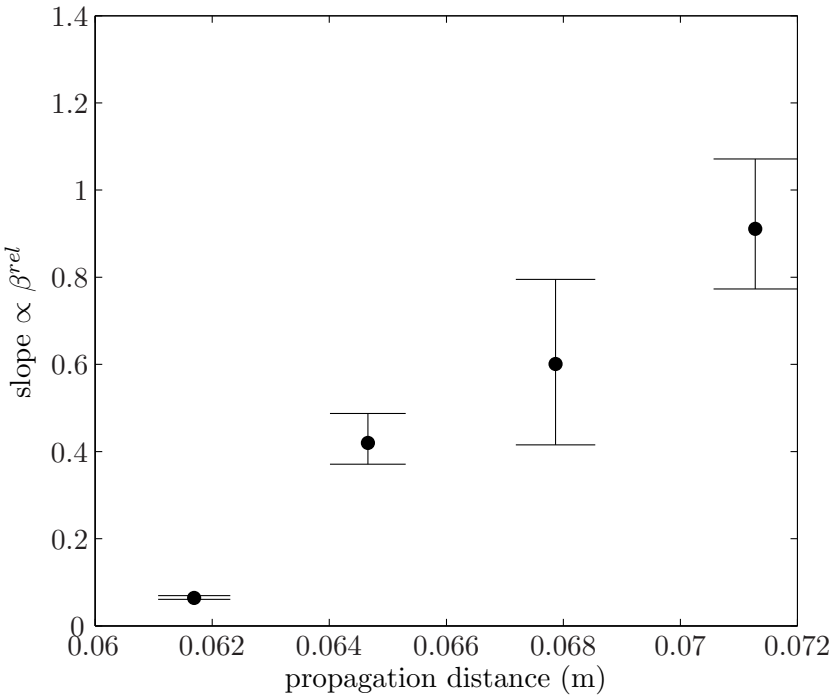

Figure 6.9: β^{rel} value measured using different incident angles plotted over propagation distance

treatments can cause differences in the nonlinearity. However, an overall agreement of the resulting nonlinearity using the reflection at a stress-free boundary in comparison to other measurement methods shows the accuracy of the proposed measurement technique, as it can be seen in Table 6.3. This result confirms that changes in the material nonlinearity can be determined with the suggested measurement setup using single-sided access to a specimen.

For the final measurement, the slope $\propto \beta^{rel}$ is determined for increasing angles, which results in increasing propagation distances. The distance between transmitting and detecting transducers is increased from 3.5 cm, 4.0 cm, 4.5 cm to 5.0 cm. The corresponding incident angle Θ_i and P-wave propagation angle Θ_P are presented in Table 6.1. For each distance six measurements are taken, where the transmitting and receiving transducers are reattached each time. The results are plotted over the propagation distance in Figure 6.9.

As expected, the β^{rel} value increases almost linearly with propagation distance. Note that this increase is not totally linear since the increasing angle causes a decreasing reflection coefficient for the reflected P-wave at the stress-free boundary. The changing reflection coefficient causes a small attenuation of the linear incline. These results are in accordance with the analytical and numerical results presented in Figure 5.10. Therefore, this last measurement setup confirms once more the coherence of analytical, numerical and experimental approach and affirms the feasibility and accuracy of the presented measurement setup using a stress-free boundary.

6.2.1 Absolute nonlinearity value

There are several works that investigate effects that have to be accounted for when evaluating the absolute nonlinearity β value. Methods to extract the absolute β value can be found in [14, 22] amongst others. Blackshire et al. [8] illustrates that beam-spreading due to diffraction effects is evident. But it is shown that the diffraction effects result in an only minor variation of less then 0.5% of the observed ratio A_2/A_1^2. Hurley and Fortunko [20] explain how to add diffraction corrections to the relative slope in order to obtain β. Diffraction and attenuation corrections are also used for calculating the absolute nonlinearity parameter in [19]. Croxford et al. [14] describe a numerical model of bulk harmonic generation which includes diffraction, attenuation and nonlinearity in a sound beam. They provide also a method to convert measured voltages to absolute amplitudes by receiver calibration and present some insights to finding the absolute β value. Similarly, Liu et al. [25] propose a scaling of the relative β value to account for damping, excitation window type and signal processing window type. In order to obtain the absolute β value, the measurement system can be calibrated by measuring β in borosilicate, which is known to have a negligible nonlinearity, as done by [22].

In summary, to obtain the absolute β value, the measure voltage has to be converted to the measured amplitude. Secondly, diffraction and attenuation corrections are necessary. Furthermore, the measurement setup has to be calibrated with borosilicate for example. This evaluation of the absolute β value is beyond the scope of this thesis. However, even

without knowing the absolute β value, the change in the nonlinearity is measured. Therefore, for monitoring the change of nonlinearity of specific in-service specimens over their lifespans, the absolute β value is not necessary. Consequently, the proposed and conducted measurement procedure can be used for monitoring the state of critical in-service components through its entire life cycle to reduce maintenance costs and to secure a higher level of safety.

CHAPTER VII

CONCLUSION AND FUTURE WORK

7.1 Conclusion

This research presents a single-sided measurement setup and measurement procedure to assess the nonlinearity of a material using the reflection at a stress-free boundary. While existing measurement setups have some drawbacks concerning single-sided measurement of in-service components, the presented measurement setup shows its potential for single-sided in-service application.

Initially, the second harmonic generation at a stress-free boundary is investigated and potential measurement setups are formulated. Two possible receiver positions are identified. The relation of second harmonic amplitude to specimen thickness, incident angle, generated incident amplitude and material nonlinearity are studied. The resulting suggested measurement method is then to choose a fixed angle, increase input amplitude and measure the slope of A_2 over A_1^2. The resulting slope is proportional to the nonlinearity of the material and can provide information about the state of the material under neutron irradiation, thermal aging or corrosion.

The theoretical results are qualitatively validated by the results of the FEM simulations taking into account the approximation and assumptions used in the analytical solution procedure. Furthermore, the results of the FEM simulations verify the suggested measurement setup and procedure and show its robustness for the size of the signal processing window and small variations of the receiver position. Additionally, the position where only the reflected P-wave arrives, referred to as position 5, is identified to be more robust and therefore the recommended receiver position. The results of the FEM simulations determine an optimal incident angle of $\Theta_P = 35° - 45°$ for that recommended receiver position. Moreover, a formula is derived for the number of generated sinus cycles for the receiver position 4, where a reflected S- as well as a reflected P-wave arrive. This formula precludes an interaction of

a diffracted P-wave with the arriving waves of interest.

Finally, experiments that comply with the simulation results confirm the feasibility of the measurement setup and the measurement procedure. The experimentally resulting acoustic nonlinearity of the measured specimen is in overall agreement with literature values. These results demonstrate accuracy and robustness of the determination of the material nonlinearity using the second harmonic generation with reflection at a stress-free boundary. Therefore, the presented measurement setup overcomes drawbacks of existing single-sided measurement setups and shows its advantages for single-sided in-service application.

7.2 Outlook

In order to further improve the repeatability of the measurement setup, an air-coupled transducer or a laser can be used to measure the particle displacement. This can eliminate some uncertainties due to coupling conditions and attachment of the receiver. Furthermore, the peak determination can be simplified by a setup with non-contact receiver.

Moreover, some investigations about diffraction correction and measurement setup calibration can be made in order to determine the absolute β value. This would enable comparing measurements results between materials as well as between different measurement methods.

REFERENCES

[1] Achenbach, J. D., *Wave Propagation in Elastic Solids*. Elsevier Science Publishers B.V., 1973.

[2] Auld, B. A., *Acoustic Fields and Waves*. John Wiley & Sons, 1973.

[3] Bender, C. M. and Orszag, S. A., *Advanced Mathematical Methods for Scientists and Engineers*. Springer-Verlag, 1999.

[4] Bender, F. A., "Analysis of second harmonic generation at a free boundary for oblique incidence," Master's thesis, Georgia Institute of Technology, 2010.

[5] Bender, F. A., Kim, J.-Y., Jacobs, L. J., and Qu, J., "The generation of second harmonic waves in an isotropic solid with quadratic nonlinearty under the presence of a stress-free boundary," *Wave Motion*, vol. 50, pp. 146–161, 2013.

[6] Bermes, C., Kim, J.-Y., Qu, J., and Jacobs, L. J., "Experimental characterization of material nonlinearity using lamb waves," *Applied Physics Letters*, vol. 90, 2007.

[7] Best, S. R., Croxford, A. J., and Neild, S. A., "Puls-echo harmonic generation measurement for non-destructive evaluation," *Journal of Nondestructive Evaluation*, vol. 32, 2013.

[8] Blackshire, J. L., Sathish, S., Na, J., and Frouin, J., "Nonlinear laser ultrasonic measurements of localized fatigue damage," *AIP Conference Proceedings*, vol. 657, pp. 1479–1488, 2003.

[9] Cantrell, J. H., *Ultrasonic Nondestructive Evaluation: Engineering and Biological Material Characterization Chapter 6*. CRC Press, 2003.

[10] Centre for Nuclear Engineering, "http://www3.imperial.ac.uk/nuclearengineering/courses/msc," accessed August 2014.

[11] Cheeke, J. . D. N., *Fundamentals and Applications of Ultrasonic Waves*. CRC Press, 2002.

[12] COMSOL, *Introduction to COMSOL Multiphysics*, version 4.4 ed., December 2013.

[13] Courant, R., Friedrichs, K., and Lewy, H., "On the prtial difference equations of mathematical physics," *IBM Journal*, pp. 215–234, 1967.

[14] Croxford, S. R. S. R. B. J. and Neild, S. A., "Modelling harmonic generation measurements in solids," *Ultrasonics*, vol. 54, pp. 442–450, 2013.

[15] Destrade, M. and Ogden, R. W., "On the third- and fourth-order constants of incompressible isotropic elasticity," *Journal of the Acoustical Society of America*, vol. 128, 2010.

[16] Ghose, B., Balasubramaniam, K., Krishnamurthy, C. V., and Rao, A. S., "Two dimensional fem simulation of ultrasonic wave propagation in isotropic solid media using comsol," tech. rep., High Energy Materials Research Laboratory, Pune, Maharashtra, India.

[17] Graff, K. F., *Wave Motion in Elastic Solids*. Oxford University Press, 1975.

[18] Herrmann, J., Kim, J.-Y., Jacobs, L. J., Qu, J., Littles, J. W., and Savage, M. F., "Assessment of material damage in a nickel-base superalloy using nonlinear rayleigh surface waves," *Journal of Applied Physics*, vol. 99, 2006.

[19] Hurley, D. C., Balzar, D., and Purtscher, P. T., "Nonlinear ultrasonic assessment of precipitation hardening in astm a710 steel," *Journal of Materials Research*, vol. 15, pp. 2036 – 2042, 2000.

[20] Hurley, D. C. and Fortunko, C. M., "Determination of the nonlinear ultrasonic parameter using a michelson interferometer," *Measurement Science and Technology*, vol. 8, p. 634?642, 1997.

[21] Jones, G. L. and Kobett, D. R., "Interaction of elastic waves in an isotropic solid," *Journal of the Acoustic Society of America*, vol. 35, 1963.

[22] Kim, J.-Y., Jacobs, L. J., and Qu, J., "Experimental characterization of fatigue damage in a nickel-base superalloy using nonlinear ultrasonic waves," *Journal of Acoustical Society of America*, vol. 120, pp. 1266–1273, 2006.

[23] Landau, L. D. and Lifshitz, E. M., *Theory of Elasticity (Course of Theoretical Physics)*. Pergamon Press, 1970.

[24] Li, P., Yost, W. T., Cantrell, J. H., and Salama, K., "Dependence of acoustic nonlinearity parameter on second phase precipitates of aluminum alloys," *IEEE 1985 Ultrasonics Symposium*, pp. 1113–1115, 1985.

[25] Liu, S., Best, S., Neild, S. A., Croxford, A. J., and Zhou, Z., "Measuring bulk material nonlinearity using harmonic generation," *NDE&E International*, vol. 48, pp. 46–53, 2012.

[26] Matlack, K. H., Wall, J. J., Kim, J.-Y., Qu, J., Jacobs, J. L., and Viehrig, H.-W., "Evaluation of radiation damage using nonlinear ultrasound," *Journal of Applied Physics*, 2012.

[27] Morlock, M. B., "Nonlinear mixing of two collinear rayleigh waves," Master's thesis, Georgia Institute of Technology, 2013.

[28] Mueller, M. F., Kim, J.-Y., Qu, J., and Jacobs, L. J., "Characteristics of second harmonic generation of lamb waves in nonlinear elastic plates," *Journal of Accoustical Society of America*, vol. 127, pp. 2141–2152, 2010.

[29] Nagy, P. B., Qu, J., and Jacobs, L. J., "Finite-size effects on the quasistatic dispalcement pulse in a solid specimen with quadratic nonlinearity," *Journal of Accoustical Society of America*, vol. 134, pp. 1760–1774, 2013.

[30] Thiele, S., Kim, J.-Y., Qu, J., and Jacobs, L. J., "Air-coupled detection of nonlinear rayleigh surface waves to assess material nonlinearity," *Ultrasonics*, vol. 54, pp. 1470–1475, 2014.

[31] van Buren, A. L. and Breazeale, M. A., "Reflection of finite-amplitude ultrasonic waves. 2. propagation," *Journal of the Acoustical Society of America*, vol. 44, pp. 1021–1027, 1968.

[32] van Buren, A. L. and Breazeale, M. A., "Reflsolids of finite-amplitude ultrasonic waves. 1. phase shift," *Journal of the Acoustic Society of America*, vol. 44, pp. 1014–1020, 1968.

[33] Yost, W. T. and Cantrell, J. H., "Effects of artificial aging of aluminum 2024 on its nonlinearity parameter," in *Review of Progress in Nondestructive Evaluation* (Thomson, D. O. and Chimenti, D. E., eds.), vol. 12, pp. 2067–2073, Plenum Press, 1993.

[34] Zhou, S. and Shui, Y., "Nonlinear reflection of bulk acoustic waves at an interface," *Journal of Applied Physics*, vol. 72, pp. 5070–5080, 1992.

[35] Zhou, S., Jiang, W., and Shui, Y., "Nonlinear bulk acoustic waves in anisotropic solids: Propagation, generation, and reflection," *Journal of Applied Physics*, vol. 78, pp. 39–46, 1995.